

## Crucial role of ring current $H^+$ in electromagnetic ion cyclotron wave dispersion relation: Results from global simulations

K. V. Gamayunov<sup>1</sup> and G. V. Khazanov<sup>2</sup>

Received 13 June 2008; revised 8 September 2008; accepted 30 September 2008; published 26 November 2008.

[1] The effect of ring current (RC)  $H^+$  in the real part of electromagnetic ion cyclotron (EMIC) wave dispersion relation is studied on the global magnetospheric scale. The simulations of the 2–3 May 1998 storm are done using our model of the  $He^+$ -mode EMIC waves self-consistently interacting with RC ions. The wave model describes EMIC waves bouncing between the off-equatorial magnetic latitudes, which correspond to the bi-ion hybrid frequencies in conjugate hemispheres, along with tunneling across the reflection zones and subsequent strong absorption in the ionosphere. This model explicitly includes the EMIC wave growth/damping, propagation, refraction, reflection, and tunneling in a multi-ion magnetospheric plasma. An analysis of the wave observations is presented and strongly supports our wave model. The main findings from our simulations can be summarized as follows: First, RC  $H^+$  only contributes a few percent to the total plasma density near the inner edge of the plasmasphere boundary layer, but it can dominate outside the plasmopause. About 90% of the RC  $H^+$  density in the dawn MLT sector is formed by the suprathermal ions ( $\approx 2$  keV), while a major contribution in dusk comes from the 10–100 keV ions, allowing not more than 10–20% for the suprathermal ions. Second, RC  $H^+$  in the real part of the wave dispersion relation increases local growth rate leading to a dramatic change in the wave global patterns. The “new” EMIC waves are generated not only on the plasmopause, as expected from previous global simulations, but also inside and outside the plasmopause consistent with the observations.

**Citation:** Gamayunov, K. V., and G. V. Khazanov (2008), Crucial role of ring current  $H^+$  in electromagnetic ion cyclotron wave dispersion relation: Results from global simulations, *J. Geophys. Res.*, 113, A11220, doi:10.1029/2008JA013494.

### 1. Introduction

[2] Electromagnetic ion cyclotron (EMIC) waves are a common feature of the Earth's magnetosphere [e.g., Anderson *et al.*, 1992a, 1992b; Erlandson and Ukhorskiy, 2001; Fraser and Nguyen, 2001]. In a number of magnetospheric regimes, the free energy for EMIC wave growth is provided by the temperature anisotropy of ring current (RC) ions, which naturally develops during inward convection from the plasma sheet. These waves have frequencies below the proton gyrofrequency, and they are excited mainly in the vicinity of the magnetic equator with a quasi-field-aligned wave normal angle [Cornwall, 1965; Kennel and Petschek, 1966]. EMIC waves strongly affect the dynamics of resonant RC ions [Cornwall *et al.*, 1970; Gonzalez *et al.*, 1989; Khazanov *et al.*, 2007b], thermal electrons [Cornwall *et al.*, 1971], thermal/suprathermal ions [Gorbachev *et al.*, 1992; Anderson and Fuselier, 1994; Fuselier and Anderson, 1996; Horne and Thorne,

1997], hot heavy ions [Thorne and Horne, 1994, 1997], and the outer radiation belt relativistic electrons [Lorentzen *et al.*, 2000; Clilverd *et al.*, 2007; Sandanger *et al.*, 2007; Summers and Thorne, 2003; Khazanov and Gamayunov, 2007], leading to nonadiabatic particle heating and/or pitch-angle scattering in the eV-MeV energy range.

[3] Starting from the pioneering work by Kennel and Petschek [1966], it is well-known that plasma density is one of the most important characteristics controlling EMIC wave generation. Assuming an electron-proton plasma, Cornwall *et al.* [1970] found that EMIC wave growth rate maximizes just inside the plasmopause, falling to zero with both decreasing (because of electron-ion collisions) and increasing L-shell (because of high critical anisotropy). In the case of a multi-ion magnetosphere, Horne and Thorne [1993] reported a result opposite to that found by Cornwall *et al.* [1970]. Namely, they found that the equatorial growth rate is substantially greater outside the plasmopause than just inside the plasmopause. They also emphasized that the local growth rate alone cannot determine the resulting wave amplification, and the propagation effects have a major impact on the path-integrated wave gain, given the path-integrated wave gain is indeed larger just inside the plasmopause. The effect of the plasmopause, and/or dayside plume, and/or detached plasma on the generation of EMIC waves is clearly seen in both the satellite data [e.g., Fraser and Nguyen, 2001; Fraser *et al.*, 2005] and the results of

<sup>1</sup>National Space Science and Technology Center, NASA, Marshall Space Flight Center, Universities Space Research Association, Huntsville, Alabama, USA.

<sup>2</sup>NASA, Goddard Space Flight Center, Greenbelt, Maryland, USA.

numerical simulations [Kozyra *et al.*, 1997; Khazanov *et al.*, 2006]. Although enhancement in the wave power was observed at the plasmopause, EMIC waves were widely seen outside the plasmopause giving an increase of the wave occurrence rate with L-shell [Anderson *et al.*, 1992a; Fraser and Nguyen, 2001]. This suggests that the plasmopause and/or the other regions of steep density gradient are not the preferred sites for wave generation.

[4] Although the effect of density on EMIC wave generation is well known, an assumption that the total plasma density is dominated by the thermal plasma was made in previous efforts to model EMIC waves on a global magnetospheric scale [e.g., Kozyra *et al.*, 1997; Jordanova *et al.*, 2001, 2006; Khazanov *et al.*, 2006]. In other words, RC ions were only included in the imaginary part of the wave dispersion relation (in growth rate) but omitted in the real part of this relation. As a result, EMIC waves were only generated near the plasmopause in all those theoretical models. The above assumption is especially severe outside the plasmopause where the RC density contribution is comparable to or even dominates the thermal plasma contribution. Therefore it is expected that RC ions in the real part of the wave dispersion relation should affect EMIC wave generation and its global distribution during active periods.

[5] Indeed, Engebretson *et al.* [2007] recently presented the Cluster observations of EMIC waves in the Pc 1–2 frequency range and associated ion distributions during the October and November 2003 storms. The most intense waves were observed on 22 November near the end of the recovery phase at L = 4.4–4.6 in the dawn MLT sector. Generation of these waves was associated with anisotropic RC  $H^+$  of energies greater than 10 keV. Although the temperature anisotropy of these energetic protons was high during the entire 22 November event, EMIC waves were observed only in conjunction with over an order of magnitude intensification of the ion fluxes below 1 keV. This suggests that a suprathermal plasma plays an important role in the destabilization of the more energetic RC and/or plasma sheet ions, and high energy anisotropic RC and/or plasma sheet protons appear to be a necessary but not sufficient condition for the occurrence of EMIC waves. Similarly, studying Pc 1–2 events in the dayside outer magnetosphere, Engebretson *et al.* [2002] and Arnoldy *et al.* [2005] found that greatly increased fluxes of low energy protons are crucial for the instability driven by anisotropic RC  $H^+$ . These observations provide strong evidence that both the cold plasmaspheric plasma and the suprathermal ( $\lesssim 1$  keV) ions injected from the plasma sheet control EMIC wave excitation. Consequently, in the present study we generalize our model of interacting RC ions and EMIC waves [Khazanov *et al.*, 2006] by taking into account RC  $H^+$  in the real part of the  $He^+$ -mode dispersion relation.

[6] This article is organized as follows: In appendix A, in order to provide an observational basis for our RC-EMIC wave model, we analyze the data currently available. In section 2, a set of governing equations is given along with the approaches and initial/boundary conditions used in the simulations of the 2–3 May 1998 storm. In section 3, an effect of plasma density on EMIC wave growth is shown for a particular event. In section 4, we analyze the plasma density distributions during 2–3 May 1998 along with a

fine energy structure of the phase space distribution function for RC  $H^+$ . In section 5, the thermal effects of RC  $H^+$  are analyzed for the  $He^+$ -mode EMIC waves. In section 6, the global distributions of the  $He^+$ -mode EMIC waves are presented and analyzed. In section 7, we discuss the satellite observations supporting our findings. Finally, in section 8 we summarize.

## 2. Equations, Approaches, and Boundary/Initial Conditions

### 2.1. Governing Equations

[7] As originally suggested in the ring current-atmosphere interaction model (RAM) [Fok *et al.*, 1993; Jordanova *et al.*, 1996], we simulate the RC dynamics by solving the bounce-averaged kinetic equation for the phase space distribution function (PSDF) of the major RC species ( $H^+$ ,  $O^+$ , and  $He^+$ ). PSDF depends on the radial distance in the magnetic equatorial plane  $r_0$ , geomagnetic east longitude  $\varphi$ , kinetic energy  $E$ , cosine of the equatorial pitch angle  $\mu_0$ , and time  $t$ , i.e.,  $F = F(r_0, \varphi, E, \mu_0, t)$ . We also use the bounce-averaged kinetic equation to describe an evolution of the wave power spectral density for the  $He^+$ -mode EMIC waves. This equation describes a physical model of EMIC waves bouncing between the off-equatorial magnetic latitudes, which correspond to the bi-ion hybrid frequencies in conjugate hemispheres, along with tunneling across the reflection zones and subsequent strong absorption in the ionosphere (for model justification see Khazanov *et al.* [2007a] and appendix A). The bounce-averaged wave kinetic equation was derived in our previous paper [Khazanov *et al.*, 2006], and it explicitly includes the EMIC wave growth/damping, propagation, refraction, reflection, and tunneling in a multi-ion magnetospheric plasma. The resulting RC-EMIC wave model based on a system of these two kinetic equations (along with a set of ray tracing equations) treats EMIC waves and RC ions self-consistently. We call this model DYNAMICS, which stands for the DYNAMIC Model of Ion Cyclotron waveS.

[8] The model governing equations have the forms:

$$\begin{aligned} \frac{\partial F}{\partial t} + \frac{1}{r_0^2} \frac{\partial}{\partial r_0} \left( r_0^2 \left\langle \frac{dr_0}{dt} \right\rangle F \right) + \frac{\partial}{\partial \varphi} \left( \left\langle \frac{d\varphi}{dt} \right\rangle F \right) + \frac{1}{\sqrt{E}} \frac{\partial}{\partial E} \\ \cdot \left( \sqrt{E} \left\langle \frac{dE}{dt} \right\rangle F \right) + \frac{1}{\mu_0 h(\mu_0)} \frac{\partial}{\partial \mu_0} \left( \mu_0 h(\mu_0) \left\langle \frac{d\mu_0}{dt} \right\rangle F \right) \\ = \left\langle \left( \frac{\delta F}{\delta t} \right)_{\text{loss}} \right\rangle, \end{aligned} \quad (1)$$

$$\begin{aligned} \frac{\partial B_w^2}{\partial t} + \langle \dot{r}_0 \rangle \frac{\partial B_w^2}{\partial r_0} + \langle \dot{\theta}_0 \rangle \frac{\partial B_w^2}{\partial \theta_0} = \left( \frac{\ln R}{T_w} + 2 \langle \gamma(r_0, \varphi, t, \omega, \theta_0) \rangle \right) \\ \cdot B_w^2(r_0, \varphi, t, \omega, \theta_0). \end{aligned} \quad (2)$$

[9] In the left-hand side of equation (1), all the bounce-averaged drift velocities are denoted as  $\langle \cdot \rangle$  and may be found in many previous papers [e.g., Khazanov *et al.*, 2003]. The term in the right-hand side of this equation includes losses from charge exchange, Coulomb collisions, RC-EMIC wave scattering, and ion precipitation to the atmosphere [e.g., Khazanov *et al.*, 2003]. Loss through

the dayside magnetopause is taken into account allowing a free outflow of RC ions from the simulation domain. In equation (2),  $\omega$ ,  $\theta_0$ ,  $\langle \dot{r}_0 \rangle$ , and  $\langle \dot{\theta}_0 \rangle$  are the wave frequency, equatorial wave normal angle, the radial velocity of the wave raypath in the equatorial plane, and the drift velocity of the equatorial wave normal angle, respectively.  $B_w$  is the wave spectral magnetic field, and  $\langle \gamma \rangle$  is a result of averaging the local growth/damping rate along the ray phase trajectory over the bounce period of the wave packet,  $T_w$ . Factor  $\langle \gamma \rangle$  takes into account both the wave energy source due to an interaction with RC ions and the energy sink due to an absorption by the thermal and hot plasmas. Tunneling of EMIC waves through the region of the bi-ion reflection is another loss mechanism included in our RC-EMIC wave model [Khazanov et al., 2006, 2007a]. This loss in equation (2) is described by the term with the reflection coefficient  $R$ , where  $(1 - R)$  gives the relative energy loss per one bounce period due to the wave tunneling (and/or mode conversion) across the off-equatorial “ion-ion hybrid latitudes.”

[10] To perform bounce averaging in equation (2), the ray phase trajectory should be known. We obtain it by solving the set of ray tracing equations. These equations can be written for a plane geometry as following [e.g., Haselgrove, 1954; Haselgrove and Haselgrove, 1960; Kimura, 1966; Khazanov et al., 2006]

$$\frac{dr}{dt} = -\frac{(\partial G / \partial \mathbf{k})_r}{\partial G / \partial \omega}, \quad (3)$$

$$r \frac{d\lambda}{dt} = -\frac{(\partial G / \partial \mathbf{k})_\lambda}{\partial G / \partial \omega}, \quad (4)$$

$$\frac{dk_r}{dt} = k_\lambda \frac{d\lambda}{dt} + \frac{(\partial G / \partial \mathbf{r})_r}{\partial G / \partial \omega}, \quad (5)$$

$$\frac{dk_\lambda}{dt} = -\frac{k_\lambda}{r} \frac{dr}{dt} + \frac{(\partial G / \partial \mathbf{r})_\lambda}{\partial G / \partial \omega}. \quad (6)$$

[11] In equations (3)–(6), the Earth-centered polar coordinate system, which characterizes any point  $P$  on the ray trajectory by the length of the radius vector  $r$  and magnetic latitude  $\lambda$ , was used. The components of the wave vector,  $k_r$  and  $k_\lambda$ , are given in a local Cartesian coordinate system centered on the current point  $P$  with its axes oriented along the radius vector and the magnetic latitude directions, respectively. The function  $G(\omega, \mathbf{k}, \mathbf{r})$  has roots for EMIC eigenmodes only, i.e.,  $G = 0$  at any point along the EMIC wave phase trajectory. Equations (3)–(6) are also used to obtain the off-equatorial EMIC wave distribution, which is needed to calculate the bounce-averaged pitch angle diffusion coefficient in the right-hand side of equation (1). For more details about system of equations (1)–(6) and its applicability please see our previous papers [Khazanov et al., 2003, 2006, 2007a] and appendix A.

[12] The pitch angle diffusion coefficient in the right-hand side of equation (1) is a functional of EMIC wave power spectral density, and  $\langle \gamma(r_0, \varphi, t, \omega, \theta_0) \rangle$  in equation (2) is a functional of PSDF. So there is a system of coupled

equations, and an entire set of equations (1)–(6) describes self-consistently RC ions and EMIC waves interacting in a quasilinear approximation.

## 2.2. Approaches Used in Simulations

[13] The geomagnetic field in our simulation is taken to be a dipole field. We use this approximation because all the results presented below are obtained from simulations of the 2–3 May 1998 period ( $Dst = -106$  nT). The Earth’s magnetic field should be slightly disturbed in the inner magnetosphere during this moderate storm [Tsyganenko et al., 2003]. We take into account the large-scale convection electric field in this study but ignore the substorm-associated field [e.g., Ganushkina et al., 2005; Goldstein et al., 2005; Mishin and Mishin, 2007; Mishin and Burke, 2005]. An effect of this substorm-associated impulsive electric field in the plasma energization, transport, and wave generation will be considered separately in the future publications. Therefore the total electric field is a sum of the convection and corotation field [e.g., Lyons and Williams, 1984]. The magnetospheric convection field is described by a shielded (exponent 2) Volland-Stern model [Volland, 1973; Stern, 1975] with its Kp dependence given by [Maynard and Chen, 1975]. For the thermal electrons, the equatorial number density is calculated using a time-dependent model of Rasmussen et al. [1993], which is also driven by Kp. To model EMIC wave propagation and interaction with RC ions, we also need to know the density distribution in the meridional plane. We employ an analytical density model that includes a product of three terms: (1) diffusive equilibrium term [Angerami and Thomas, 1964], (2) the lower ionosphere term, and (3) the plasmapause and the outer magnetosphere term. This analytical model is adjusted to the Rasmussen et al. model in the equator plane. So the resulting plasmaspheric density model provides a three-dimensional spatial distribution for electrons. The ion content in our simulations is assumed to be 77%  $H^+$ , 20%  $He^+$ , and 3%  $O^+$ . Geocoronal neutral hydrogen density, needed to calculate loss due to charge exchange, is obtained from a spherically symmetric model of Chamberlain [1963] with its parameters given by Rairden et al. [1986].

[14] During the main phase of major storms, RC  $O^+$  may dominate [e.g., Hamilton et al., 1988; Daglis, 1997] and, as a result, contributes to a strong damping of the  $He^+$ -mode EMIC waves [Thorne and Horne, 1997]. Although this process is important in principle, let us evaluate the validity of excluding RC  $O^+$  in the 2–3 May 1998 storm simulation. Farrugia et al. [2003] found that the energy density of RC  $H^+$  is greater than twice that of  $O^+$ , and that the contribution of  $He^+$  to the RC energy content is negligible during the strongest second main phase on 4 May 1998 ( $Dst = -272$  nT). This implies that the RC  $O^+$  content does not exceed 30% during the second main phase of the May 1998 storm. This estimate was obtained from a global simulation using the RC model of Jordanova et al. [1998], which did not include the oxygen band waves, and it is likely that Farrugia et al. [2003] overestimated the RC  $O^+$  content during 4 May 1998. Indeed, Bräysy et al. [1998] observed very asymmetric  $O^+$  RC during the main phase of the 2–8 April 1993 storm, which suggests that the RC  $O^+$  loss rate is considerably faster than the drift speed. This result is difficult to explain in terms of charge exchange and Cou-



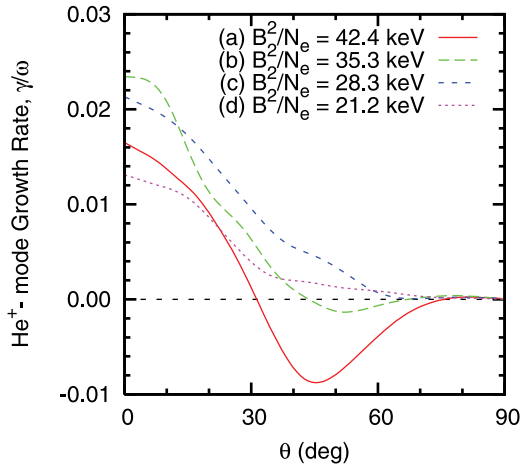


**Figure 1.** The equatorial growth/damping rate versus wave normal angle for the  $He^+$ -mode EMIC waves. The RC is assumed to be entirely made up of energetic protons, and the thermal plasma consists of the cold electrons, 77%  $H^+$ , 20%  $He^+$ , and 3%  $O^+$ . All the results are obtained for the wave frequency  $\nu = \omega/2\pi = 0.475$  Hz, and the RC  $H^+$  PSDF is taken from our global simulation at  $L = 5.25$ , MLT = 15 ( $B = 215.3$  nT), and hour 48 after 0000 UT on 1 May 1998. (a) The electron number density is also determined by the global model, and  $N_e = N_0 = 68.3 \text{ cm}^{-3}$  (nominal case). In order to generate results (b, c, and d), we kept all the parameters as in case a except the electron number densities  $N_e = 1.2N_0$ ,  $N_e = 1.5N_0$ , and  $N_e = 2N_0$  respectively were adopted.

lomb scattering, and suggests that the production of EMIC waves contributes significantly to the RC  $O^+$  decay during the main and early recovery phases. In other words, due to the generation of the  $O^+$ -mode EMIC waves, most RC  $O^+$  precipitates before reaching the dusk MLT sector [Bräysy *et al.*, 1998]. Therefore to estimate the RC  $O^+$  content correctly, the  $O^+$ -mode EMIC waves should be included in the simulation. In any case, the calculations of Thorne and Horne [1997] clearly demonstrated that even the RC  $O^+$  percentage noted above cannot significantly suppress the  $He^+$ -mode amplification, and only slightly influences the resulting growth; inclusion of 26%  $O^+$  in the RC population causes the net wave gain decrease by only 20%. Moreover, in the present study we simulate the 2–3 May 1998 period, i.e., the first main ( $Dst = -106$  nT) and recovery phases of the May 1998 large storm, when the RC  $O^+$  content must be even smaller than the above estimate for 4 May 1998. It is for these reasons that we chose to exclude RC  $O^+$  in our simulations of 2–3 May 1998, and to assume that RC is entirely made up of energetic protons.

[15] Finally, following our previous approach [Khazanov *et al.*, 2006, 2007b], we ignore the wave packet radial drift and tunneling. Consequently,  $\langle \dot{r}_0 \rangle = 0$  and  $R = 1$  in equation (2), and below we will use a truncated wave kinetic equation.

### 2.3. Boundary and Initial Conditions

[16] The night-side RC boundary condition is imposed at the geostationary distance. We use the flux measurements from the Magnetospheric Plasma Analyzer, and the Syn-

chronous Orbit Particle Analyzer instruments on the geosynchronous LANL satellites during the modeled event. Then, according to Young *et al.* [1982], we divide the total flux measured at geostationary orbit between RC  $H^+$ ,  $O^+$ , and  $He^+$  depending on geomagnetic and solar activity as measured by the  $Kp$  and  $F_{10.7}$  indices. Only the  $H^+$  fluxes are used as a boundary condition because the RC  $O^+$  and  $He^+$  contributions can be neglected in this particular study.

[17] To obtain the self-consistent initial conditions for equations (1) and (2), the simulation was started at 0000 UT on 1 May 1998 using a background noise level for the  $He^+$ -mode EMIC waves [e.g., Akhiezer *et al.*, 1975b], the statistically derived quiet time RC  $H^+$  energy distribution of Sheldon and Hamilton [1993], and the initial pitch angle characteristics of Garcia and Spjeldvik [1985]. The initial RC and EMIC wave distributions are derived independently and, moreover, they have nothing to do with a particular state of the magnetosphere during a simulated event. Only the boundary conditions provided by LANL and, to a certain extent, the employed plasmaspheric and electric/magnetic field models can be considered as an input reflecting a particular geomagnetic situation. Therefore before simulation of a particular geomagnetic event can be possible, one first seeks an initial state for RC and EMIC waves, which is self-consistent and reflects the particular geomagnetic situation. In our case, this was done by running the model code for 24 hours. In about 20 hours of evolution, the wave energy distribution reaches a quasi-stationary state indicating that an entire RC-EMIC wave system achieves a quasi-self-consistent state. Note that these 20 hours have nothing to do with a typical time for wave amplification, but instead reflect the minimum time needed to adjust RC and waves to each other and to a real prehistory of the storm. So a self-consistent modeling of the 2–3 May 1998 storm period is started at 0000 UT on 2 May (24 hours after 1 May, 0000 UT) using solutions of equations (1) and (2) at 2400 UT on 1 May as the initial conditions for further simulation.

### 3. Effect of Number Density on EMIC Wave Growth

[18] The effective proton temperatures transverse to ( $T_\perp$ ) and along ( $T_\parallel$ ) the field line comply with an inequality  $T_\perp > T_\parallel$  in many space plasma regimes. If the temperature anisotropy ( $A = T_\perp/T_\parallel - 1$ ) of RC ions exceeds some positive threshold, EMIC waves can be unstable [Kennel and Petschek, 1966; Cornwall *et al.*, 1970]. The instability growth rate strongly depends on the so-called proton characteristic energy for cyclotron interaction, which is the energy of the external magnetic field per one particle, i.e.,  $E_c = B^2/(8\pi N_e)$  [Kennel and Petschek, 1966]. So the local growth rate of EMIC waves should be particularly sensitive to the local plasma density. Assuming that RC is entirely made up of energetic  $H^+$ , Figure 1 shows the dependence on plasma density the equatorial growth/damping rate for the  $He^+$ -mode EMIC waves. Note that the growth/damping rates in Figure 1 are due to the RC-EMIC wave interaction only, and the wave absorption by thermal plasma is omitted (of course, this is included in our global simulations). All the results in Figure 1 are obtained for the wave frequency  $\nu = 0.475$  Hz and case (a) is just

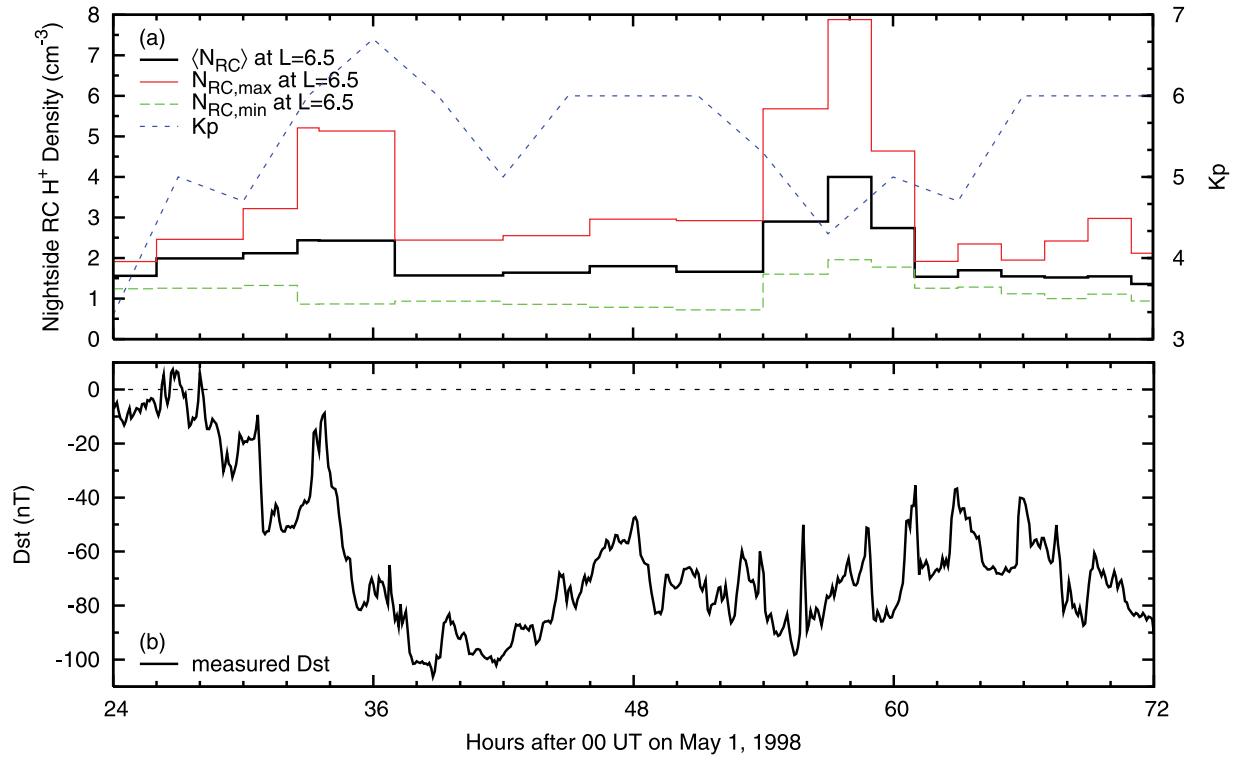


**Figure 2.** (a) The RC  $H^+$  number density in the nightside at  $L = 6.5$  during 2–3 May 1998. The density averaged over MLT = 18–06, the nightside maximum, and minimum densities are shown as  $\langle N_{RC} \rangle$ ,  $N_{RC,max}$ , and  $N_{RC,min}$ , respectively. The plotted Kp index is an indicator of strength of the magnetospheric convection. (b) Measured Dst index.

taken from our modeling at  $L = 5.25$ , MLT = 15, and hour 48 ( $N_e = N_0 = 68.3 \text{ cm}^{-3}$ ,  $B = 215.3 \text{ nT}$ ) without any modification. To produce the results (b), (c), and (d), we only renormalized the local plasma density as  $N_e = 1.2 N_0$ ,  $N_e = 1.5 N_0$ , and  $N_e = 2.0 N_0$ , respectively. As follows from Figure 1, transition from case (a) to case (b) increases the peak growth rate by factor 1.4, extends the region of growth, and makes negligible the wave damping. The further plasma density increase eliminates the region of wave damping. To understand the dependences shown in Figure 1, let us recall that the wave growth rate depends on plasma density as  $\gamma \sim \exp(-1/N_e)/\sqrt{N_e}$ , i.e., has a maximum for some particular  $N_e$  if the other plasma and all the wave parameters are fixed [e.g., Kennel and Petschek, 1966]. Therefore although the characteristic energy decreases with plasma density, the growth rate can both increase or decrease depending on the wave normal angle (the rest of parameters are fixed in Figure 1). For a particular wave normal angle, it depends on whether we move to the growth rate maximum with density increase or whether we move from the maximum. A strong sensitivity of the wave growth rate to plasma density is a key point for the present study.

[19] What we have shown above is a well-known fact, and RC ions are usually included in both the real and imaginary parts of the wave dispersion relation in order to study the wave dispersive properties [e.g., Kozyra et al., 1984; Gamayunov et al., 1993]. Despite that, to the best of our knowledge, all previous efforts to model EMIC waves on the global magnetospheric scale included RC ions in the

imaginary part of the wave dispersion relation only. RC ions in the real part of the wave dispersion relation will affect EMIC wave generation and its global distribution during the storm, and our self-consistent RC-EMIC wave model is an appropriate tool to study this effect on the global magnetospheric scale.

## 4. Plasma Density Distribution and Energy Spectrum of RC $H^+$

### 4.1. Plasma Density Distribution During 2–3 May 1998

[20] Let us first consider a number density distribution of RC  $H^+$  on the nightside geostationary boundary. To provide an overall insight, we calculated the RC density at  $L = 6.5$  and then averaged it over all the nightside MLTs (18–06). We also kept the maximum and minimum RC densities on the nightside geostationary boundary. The results of our calculation are shown in Figure 2. To provide a qualitative assessment of the magnetospheric convection strength, we plotted the Kp index in Figure 2a. Note that the plotted Kp index is a linear interpolation of the 3-hour Kp index, and this interpolation was actually used in the simulations. During hours 24–36, both the Kp index and RC density grow strongly maximizing at  $Kp = 7^-$  and  $N_{RC,max} = 5.2 \text{ cm}^{-3}$  (MLT = 05), respectively. After hour 42, Kp starts to grow again but the RC density grows only slightly being, on average, about  $\langle N_{RC} \rangle = 1.7 \text{ cm}^{-3}$ . The striking feature is observed after hour 51 when Kp decreases from 6 to 4<sup>+</sup>, while the RC density grows sharply maximizing at

May 2–3, 1998: RC Proton Density

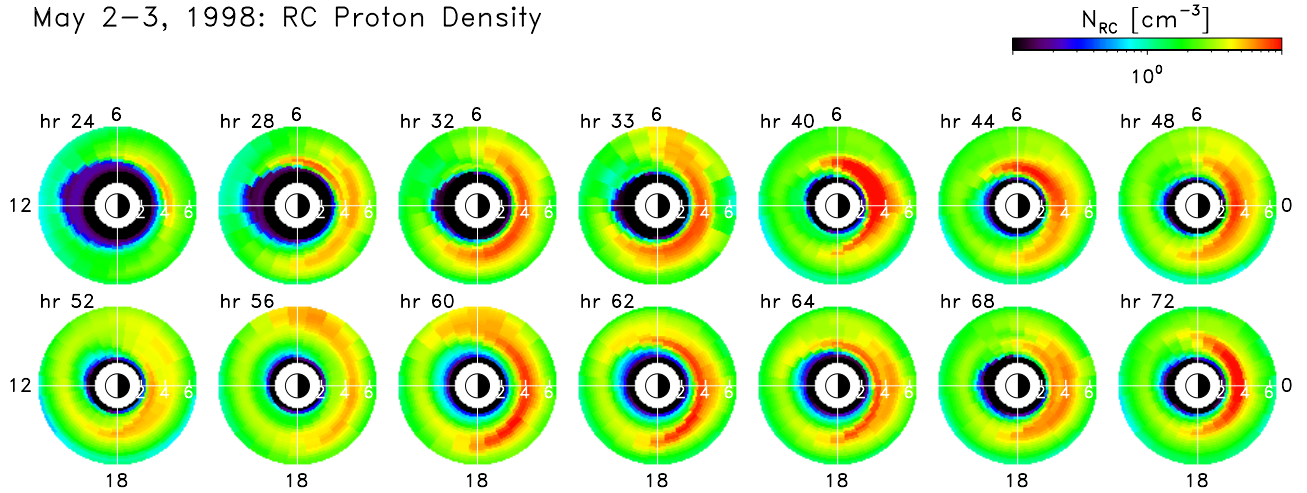


**Figure 3.** The RC  $H^+$  density distribution in the equatorial plane during 2–3 May 1998. The plasma sheet ion injections are seen at hours 28, 33, 44, 56, and 64. All the hours are counted from 0000 UT on 1 May 1998.

$N_{RC,max} = 7.9 \text{ cm}^{-3}$  (MLT = 05) near hour 58 that correlates with an elevated solar wind density [e.g., Khazanov *et al.*, 2003]. The last RC density intensification starts at hour 63 from  $N_{RC,max} = 1.9 \text{ cm}^{-3}$  followed by a moderate density increase up to  $N_{RC,max} = 3.0 \text{ cm}^{-3}$  at hour 70. This intensification is again accompanied by growth of Kp. So during 2–3 May 1998, we can identify four periods of the plasma sheet density increase on the nightside geostationary boundary. The magnetospheric convection field is strengthening during three of these periods, but the greatest plasma sheet density

enhancement during hours 54–61 takes place for a period of decreasing Kp.

[21] Both the plasma sheet density enhancement and the convection field intensification affect RC density in the inner magnetosphere. To provide a global view of the RC density evolution inside geostationary orbit, we selected fourteen snapshots of the equatorial density distribution during 2–3 May 1998, which are shown in Figure 3. The plasma sheet ion injections are clearly seen in the inner magnetosphere snapshots at hours 28, 33, 44, 56, and 64, which are in agreement with the geostationary density

May 2–3, 1998: RC  $H^+$ , Thermal, and Sum of Thermal and RC  $H^+$  Plasma Densities

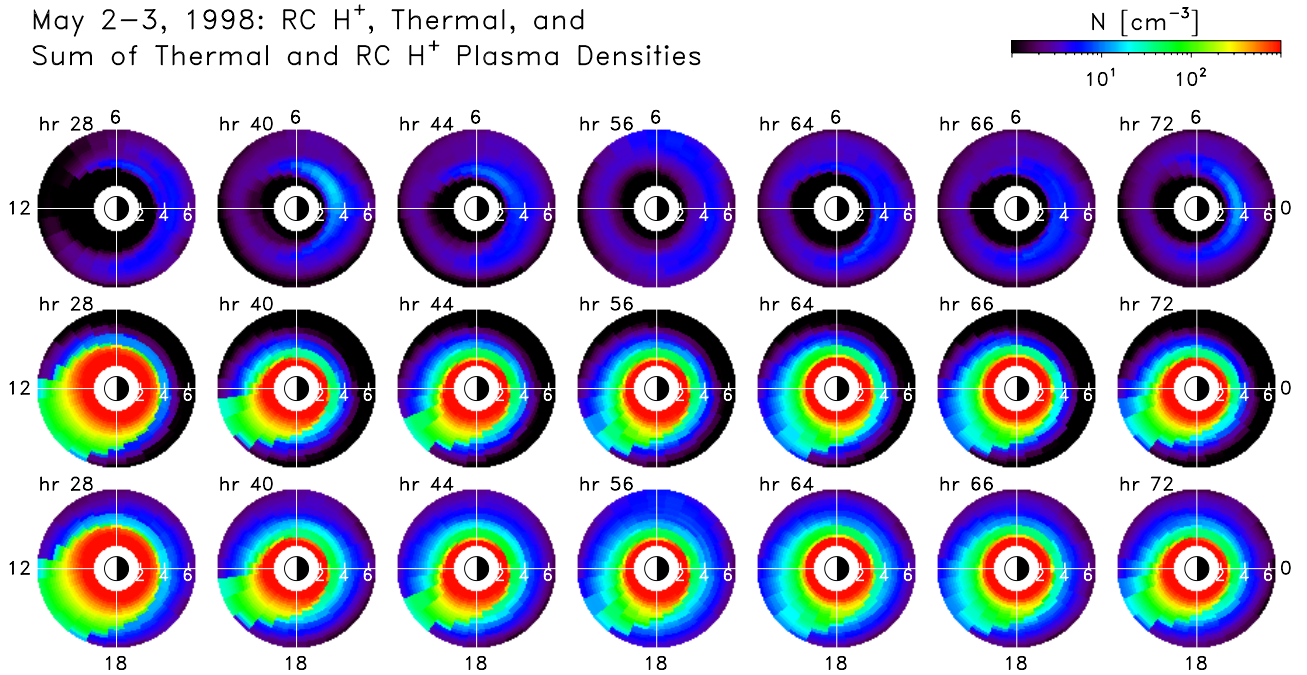


**Figure 4.** The equatorial plasma density distributions during 2–3 May 1998. The first, second, and third rows show the simulated RC  $H^+$  density, the cold electron density from the Rasmussen *et al.* model, and a sum of the thermal plasma and RC  $H^+$  densities respectively. Note that compared to Figure 3, we used a different color scale here.

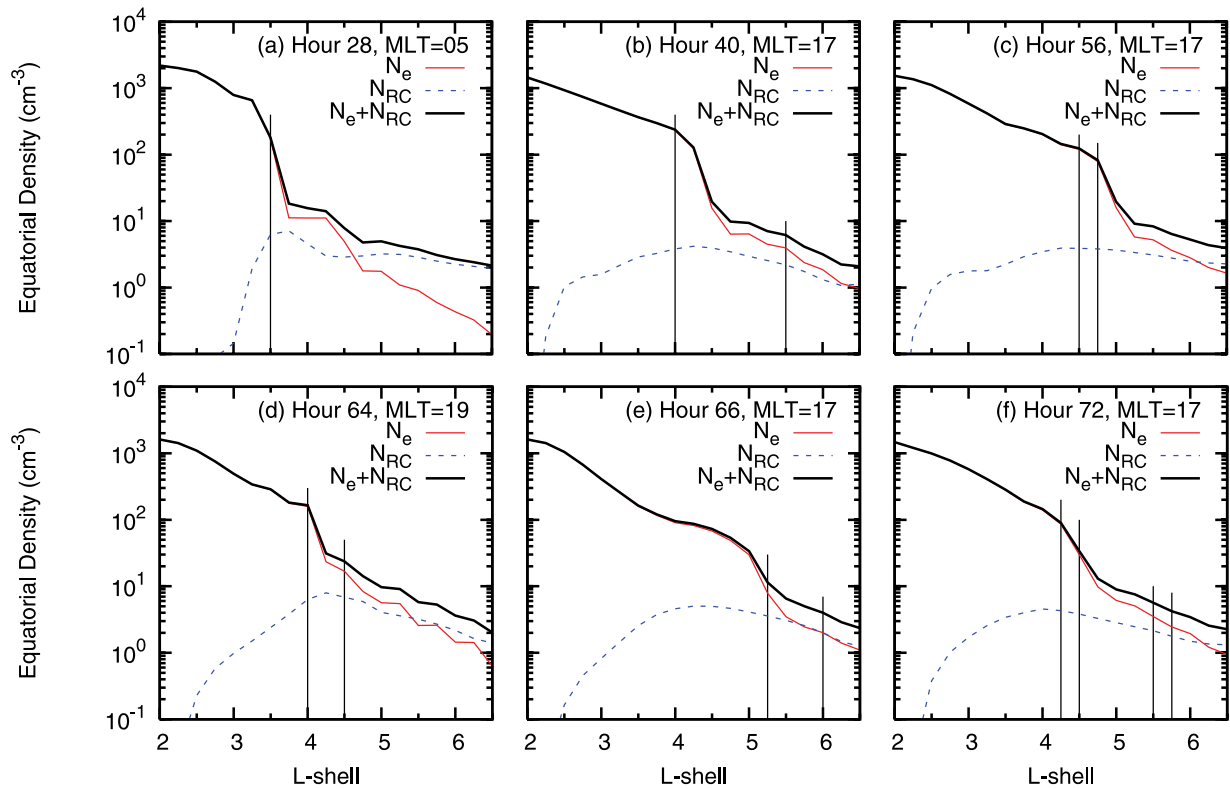


**Figure 5.** The equatorial plasma density versus L-shell for representative hours and MLTs. The density profiles for the thermal plasma, RC  $H^+$ , and a sum of the thermal plasma and RC  $H^+$  are shown. The vertical lines mark positions where an inclusion of RC  $H^+$  in the real part of the wave dispersion relation makes possible the  $He^+$ -mode EMIC wave generation compared to the case when RC ions are only included in the imaginary part of the wave dispersion relation.

distribution shown in Figure 2a. The most intense RC is observed at hour 40 during the very early recovery phase (see Figure 2b) when the dense RC is encircling an entire night sector maximizing at  $N_{RC} = 10\text{--}17 \text{ cm}^{-3}$  in the premidnight-dawn sector for  $L = 3\text{--}3.75$ . During the following storm recovery, a moderate injection of the plasma sheet material is observed near hour 44 and, starting at hour 48, we can see a short period of the  $Dst$  decrease (see Figure 2b). The greatest plasma sheet density enhancement during hours 54–61 (see Figure 2a) causes the RC density enhancement as seen in Figure 3, in snapshots for hours 56–62. The RC density maximizes at  $N_{RC} = 7\text{--}10 \text{ cm}^{-3}$  in the night MLT sector during hours 60–62. The last RC intensification shown in Figure 3 appears at hour 64 and, as seen in the hour 72 snapshot, the RC density attains a maximum at  $N_{RC} \approx 13 \text{ cm}^{-3}$  near midnight for  $L = 3.25\text{--}3.5$ .

[22] The equatorial density distributions of RC  $H^+$ , thermal electrons, and a sum of the thermal plasma and RC  $H^+$  are plotted in Figure 4. Note that, compared to Figure 3, we used a different color scale in Figure 4. RC  $H^+$  dominates the thermal plasma density starting from some L-shell outside the plasmapause except for a dayside plasmaspheric drainage plume. Overall, we see that RC  $H^+$  makes the shape of the “thermal” plasmapause smoother and the plasmasphere boundary layer less steep. To show a fine density structure in the distributions shown in Figure 4, we selected six meridional cuts, which are representative among the cases in which an inclusion of RC  $H^+$  in the

real part of the wave dispersion relation strongly affects the  $He^+$ -mode EMIC waves (see section 6). The corresponding equatorial plasma density profiles are shown across the entire simulation domain in Figure 5. It is seen that RC  $H^+$  affects the total density distribution outside the innermost edge of the plasmasphere boundary layer only making, on average, the density gradients more shallow.

[23] So far, we only discussed the RC  $H^+$  density distribution and did not say anything about distribution of electrons. It is obvious that a quasineutrality condition must hold in the “slow” magnetospheric processes. Quasineutrality can be sustained by both the energetic plasma sheet electrons injected along with the plasma sheet ions, and/or the cold ionospheric electrons due to the field-aligned currents. An effective temperature of this hot-cold electron mixture strongly affects the Coulomb energy degradation of RC ions and the resonant Landau damping of EMIC waves, but barely influences the EMIC wave dispersive properties [e.g., Khazanov *et al.*, 2007b; Akhiezer *et al.*, 1975a]. We previously demonstrated that the  $He^+$ -mode EMIC wave Landau damping and collisional RC energy dissipation are both maximized for an electron temperature about 1 eV [Khazanov *et al.*, 2007b]. This is a temperature of the thermal plasma currently adopted in our RC-EMIC wave model [e.g., Khazanov *et al.*, 2003]. Therefore if we do not track an electron dynamics but rather keep  $T_e = 1 \text{ eV}$  in an entire simulation domain, we potentially underestimate energy of the resulting waves, especially at high L-shells



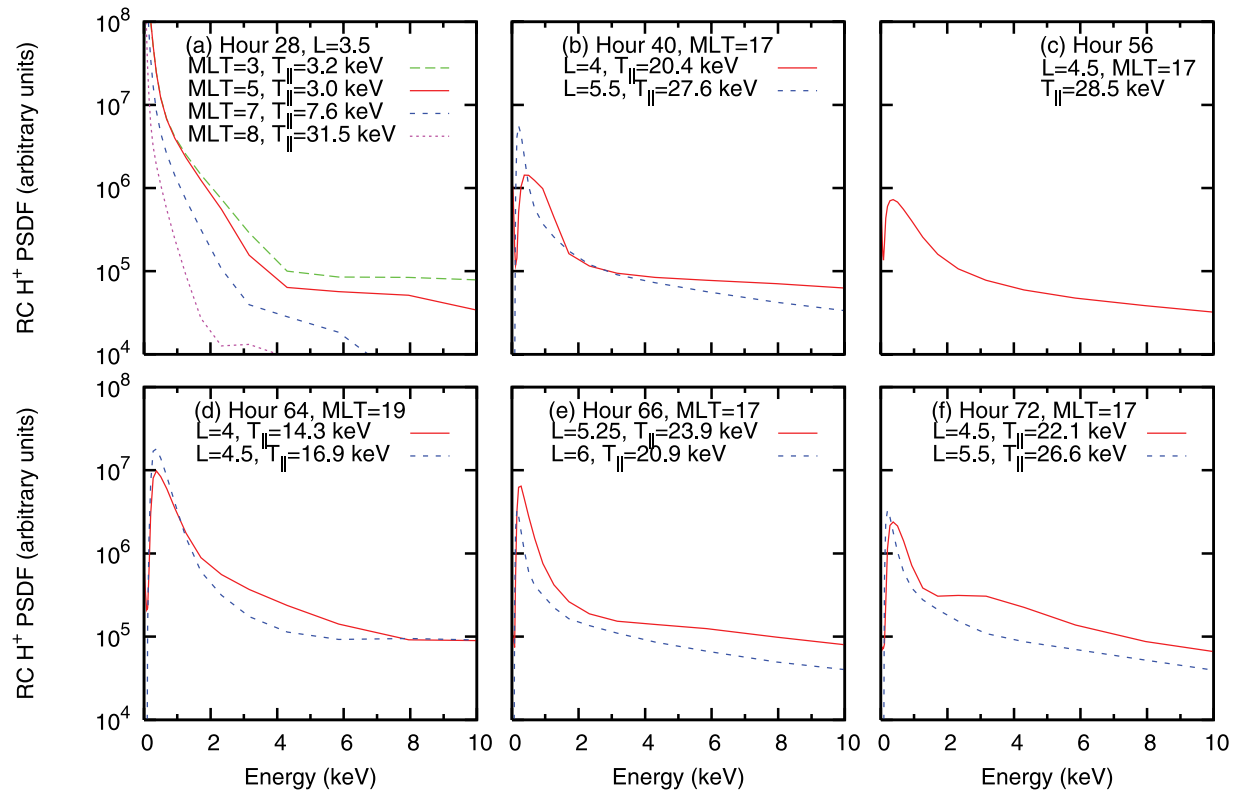


**Figure 6.** The simulated PSDFs for RC  $H^+$ . All the PSDFs are shown in the equatorial plane and integrated over the entire solid angle. The corresponding parallel proton temperature  $T_{||}$  is calculated for the entire energy range 0.1–430 keV. Note that only spectra below 10 keV are shown.

during the main and recovery storm phases when RC ions dominate thermal plasma. This is due to the larger Landau damping for waves and the greater Coulomb energy degradation for RC ions. In the present study we adopt this conservative approach, and assume an electron temperature of 1 eV throughout the entire simulation domain.

#### 4.2. RC $H^+$ Energy Spectrum

[24] As shown in Figure 3, the new RC  $H^+$ , injected from the plasma sheet in the night MLT sector, causes the plasma density enhancement in the inner magnetosphere during the main and recovery storm phases. All those RC density distributions are calculated for the entire energy range 0.1–430 keV adopted in our model, and do not provide us with the information whether the total RC  $H^+$  density is formed by the entire PSDF or whether there is one (or a few) RC  $H^+$  subpopulation, which primarily contributes to a total density. To get such insight, we first consider the energy distribution of RC  $H^+$  during 2–3 May 1998. For consideration, we selected the cases marked by the vertical lines in Figure 5, i.e., the representative cases in which an inclusion of RC  $H^+$  in the real part of the wave dispersion relation strongly affects the  $He^+$ -mode EMIC waves. The selected thirteen PSDFs are shown in Figure 6. Note that Figure 6a shows three extra distributions in vicinity of the marked point in Figure 5a, while Figures 6c and 6f show only one PSDF for each pair of the vertical lines shown in Figures 5c and 5f. PSDFs are taken in the equatorial plane and integrated over an entire solid angle. An effective RC  $H^+$  temperature along the magnetic field,  $T_{||}$ , is calculated

for the entire energy range. All the energy spectra shown are similar to each other except the dawn spectra reach maximum at the low energy edge (Figure 6a) whereas all the dusk spectra do not have such low energy ions. A general feature seen in all spectra is a transition from steep profile to a more shallow gradient that corresponds to a transition from the small to a higher effective temperature. So we observe at least two ion populations, which constitute the plotted PSDFs: (1) the relatively cool low energy RC component and (2) the more hot higher energy RC component. As follows from Figure 6, the boundary between these two RC  $H^+$  components is located at slightly different energy, which is about 2 keV or less, depending on the case.

[25] Figure 6 cannot tell us whether the low energy RC component dominates the total RC density or whether the high energy fraction does (except for Figure 6a where the total density is likely formed by the cool low energy component). To obtain the needed information, we calculate a fraction of the total RC  $H^+$  density accumulated in the energy range 0.1 keV –  $E$  versus  $E$ . Results of our calculations are plotted in Figure 7. It is seen that the total RC density is dominated by the suprathermal ions in the dawn MLT sector; it follows from Figure 7a that 90% of the RC density is formed by  $H^+$  with  $E \lesssim 2$  keV and a secondary contribution from protons with  $E > 100$  keV is clearly observed for MLT = 7, and especially for MLT = 8. On the other hand, as follows from Figures 7b–7f, energetic  $H^+$  contributes mostly to the total RC density in the dusk sector where a density level of 90% is reached at about



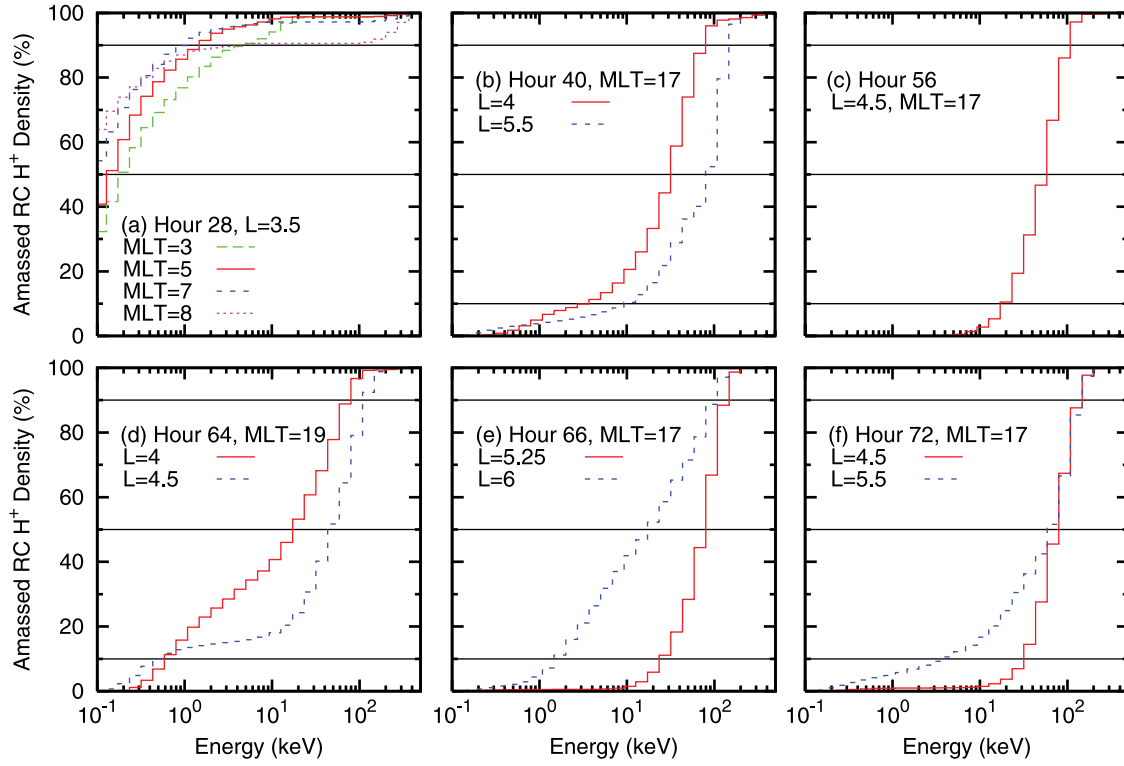


**Figure 7.** An amassed fraction of the RC  $H^+$  density versus energy. The horizontal lines mark the density levels of 10, 50, and 90 percent. All the shown combinations of hours, L-shells, and MLTs are the same as in Figure 6.

100 keV but RC  $H^+$  with energy  $\lesssim 1$  keV does not contribute more than 10–20%. So the results in Figure 7 demonstrate that plasma density modification, due to the plasma sheet  $H^+$  injection into the RC region, is primarily caused by low energy ions ( $\lesssim 2$  keV) in the dawn MLT sector and the 10–100 keV ions in dusk.

## 5. Effect of RC $H^+$ Temperature on $He^+$ -Mode EMIC Wave Dispersive Properties

[26] Let us first recall that RC  $H^+$  dominates both RC  $O^+$  and  $He^+$  during 2–3 May 1998 (see section 2.2), and we neglect the RC heavy ions in the present study. Second, despite a potential importance of RC ions for the EMIC wave dispersive characteristics [e.g., Kozyra *et al.*, 1984], in all previous studies we assumed that the total ion composition is determined by an ion composition of the thermal plasma [e.g., Khazanov *et al.*, 2006, 2007b]. In other words, we did not take into account RC ions in the real part of the wave dispersion relation, including them in the imaginary part only. Now we consider the effect of RC  $H^+$  in the real part of the  $He^+$ -mode EMIC wave dispersion relation. This modifies the percentage of all ions. Despite that, for the purpose of comparison with our previous results, we keep the earlier adopted ion percentage (77%  $H^+$ , 20%  $He^+$ , and 3%  $O^+$ ) throughout the entire simulation domain even if the percentage is mainly determined by suprathermal/hot ions.

[27] Although we demonstrated in section 4.2 that the plasma density enhancement is caused by suprathermal ( $\lesssim 1$  keV) RC  $H^+$  population in the morning MLT sector, and the 10–100 keV ions in the dusk, this does not allow us

to assess an effect of the RC  $H^+$  temperature in the EMIC wave dispersion relation. To evaluate this effect, the following parameters,

$$\lambda_{H^+} = \left( \frac{k_{\perp} v_{\perp, H^+}}{\sqrt{2} \Omega_{H^+}} \right)^2, \quad \zeta_{H^+} = \left( \frac{\omega \pm \Omega_{H^+}}{k_{\parallel} v_{\parallel, H^+}} \right)^2, \quad (7)$$

may be analyzed [e.g., Stix, 1992; Akhiezer *et al.*, 1975a]. In equation (7),  $\Omega_{H^+}$  is the proton gyrofrequency,  $k_{\perp}$  ( $v_{\perp, H^+} = \sqrt{2T_{\perp, H^+}/m_{H^+}}$ ) and  $k_{\parallel}$  ( $v_{\parallel, H^+} = \sqrt{2T_{\parallel, H^+}/m_{H^+}}$ ) are the components of the wave normal vector (thermal velocity) transverse to and along geomagnetic field lines, respectively,  $\lambda_{H^+}$  is the squared ratio of Larmor radius to transverse wavelength, and  $\zeta_{H^+}$  is the squared ratio of the longitudinal wavelength to a typical ion displacement along the field line during one wave/gyro period. An effect of the finite Larmor radius is negligible if  $\lambda_{H^+} \ll 1$ . On the other hand, RC  $H^+$  becomes unmagnetized if  $\lambda_{H^+} \gg 1$  and, as a consequence, the external magnetic field disappears in the RC terms in the wave dispersion relation. So the finite Larmor radius effect is important for an intermediate case when the wave and plasma parameters give  $\lambda_{H^+} \sim 1$ . The magnitude of  $\zeta_{H^+}$  characterizes not only an importance of the “longitudinal” thermal effect but also determines the effectiveness of the wave resonant growth/damping. For instance, the number of resonant particles is small if  $\zeta_{H^+} \gg 1$  and, as a result, plasma waves can exist for a long time without an essential damping/growth. The role of thermal effects in the wave dispersion relation depends on the magnitude of both  $\zeta_{H^+}$  and  $\lambda_{H^+}$ . For example, if these parameters comply with the inequalities  $\lambda_{H^+} \ll 1$  and  $\zeta_{H^+} \gg 1$ , in many cases (but not always) the leading term in

May 2–3, 1998: B-field Spectrogram  
Without and With RC  $H^+$  Ions in Dispersion Relation

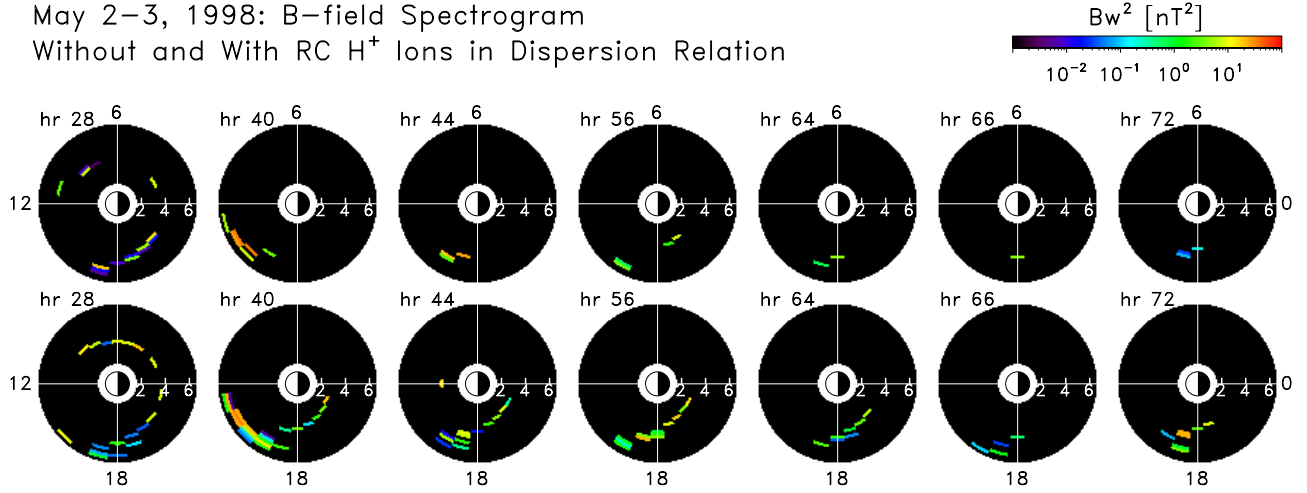


**Figure 8.** The equatorial distribution of the squared wave magnetic field of the  $He^+$ -mode EMIC waves during 2–3 May 1998. The results are obtained by solving equations (1)–(6). The first row shows the case when RC  $H^+$  is only treated as a source of free energy to generate waves and omitted in the real part of the wave dispersion relation. The second row demonstrates distributions when RC  $H^+$  is taken into account in both the real and imaginary parts of the wave dispersion relation.

the real part of the wave dispersion relation still comes from a cold plasma limit, i.e., from the limit  $\lambda_{H^+} = 0$  and  $\zeta_{H^+} = \infty$  [e.g., Stix, 1992]. So depending on the magnitudes of  $\zeta_{H^+}$  and  $\lambda_{H^+}$ , the thermal terms may be a minor correction to or they can dominate the cold plasma limit term.

[28] As follows from Figure 5, RC  $H^+$  affects the total density only outside the innermost edge of the plasmasphere boundary layer. It allows us to evaluate the above parameters in this region only. Because the Alfvén velocity increases with L-shell, parameter  $\lambda_{H^+}$  ( $\zeta_{H^+}$ ) decreases (increases) with L-shell, having a maximum (minimum) at the innermost edge of the plasmasphere boundary layer. Analysis during the 2–3 May 1998 period shows that inequality

$$\max[\lambda_{H^+}] \ll 1 \ll \min[\zeta_{H^+}] \quad (8)$$

holds for the  $He^+$ -mode EMIC waves in the entire region outside the innermost edge of the plasmasphere boundary layer. Note that  $v_{\perp, H^+}$  and  $v_{\parallel, H^+}$ , needed to calculate parameters  $\lambda_{H^+}$  and  $\zeta_{H^+}$ , were evaluated for the entire energy range 0.1–430 keV, and both of the above inequalities become stronger outside the plasmopause. These inequalities (equation (8)) suggest that in order to evaluate the RC  $H^+$  terms in the  $He^+$ -mode EMIC wave dispersion relation we may use the cold plasma approximation ( $\zeta_{H^+} \gg 1$ ) for the plasma dispersion function [e.g., Stix, 1992], and the effect of the finite Larmor radius may be neglected [e.g., Akhiezer et al., 1975a]. In the cold plasma approximation, one term is purely “cold,” and so its contribution is identical to that of the plasmaspheric protons (except number density). The other one, which includes the RC  $H^+$  temperature, has a different form. The structure of both these terms can be found in many plasma physics monographs [e.g., Stix, 1992].

[29] As we previously emphasized, the validity of the cold plasma approximation does not guarantee that the thermal term in the wave dispersion relation is only a minor

correction to the cold plasma limit term. Therefore a comparison of these two terms is required. To do so we again consider only the region outside the innermost edge of the plasmasphere boundary layer. A relative contribution of the thermal term increases with L-shell, having minimum near the innermost edge of the plasmasphere boundary layer. Taking the total “cold” contribution from all plasma species (thermal and RC  $H^+$ ) as a unit, we found that the RC  $H^+$  thermal contribution to the  $He^+$ -mode EMIC wave dispersion relation,  $\Lambda_{H^+}$ , satisfies the inequality

$$\max[\Lambda_{H^+}] \ll 1. \quad (9)$$

Inequality (9) means that, compared to the total “cold” contribution, the RC  $H^+$  thermal term may be omitted in the  $He^+$ -mode EMIC wave dispersion equation, at least in simulations of the 2–3 May 1998 storm. In other words, RC  $H^+$  can be safely treated as the “cold” ions in the real part of the wave dispersion relation, and the RC  $H^+$  temperature is only needed in the imaginary part of the wave dispersion relation.

## 6. Global Distribution of $He^+$ -Mode EMIC Waves

[30] The equatorial distributions of the squared wave magnetic field,

$$B_w^2(r_0, \varphi, t) = \int_{\omega_{\min}}^{\omega_{\max}} d\omega \int_0^\pi d\theta_0 B_w^2(r_0, \varphi, t, \omega, \theta_0), \quad (10)$$

are shown in Figure 8 for the  $He^+$ -mode EMIC waves. The distributions in the first row are obtained from the simulation when RC  $H^+$  is only treated as a source of free energy for the EMIC wave generation and omitted in the real part of the wave dispersion relation. The second row is for the case when RC  $H^+$  is taken into account in both the real and imaginary parts of the wave dispersion relation. There are clearly more waves in the second row compared

to the first one. The reason for that is an increase of the local growth rate caused by increase of the total density (see Figure 1). Indeed, it was shown in section 4.1 that an inclusion of RC  $H^+$  in the global density model makes the density gradients more shallow outside the innermost edge of the plasmasphere boundary layer (see Figures 4 and 5). This suggests that the density gradient becomes less effective to counteract the wave refraction caused by the magnetic field gradient/curvature. Therefore the much greater wave activity observed in the second row of Figure 8 is due to an increase of the local growth rate that overshoots the increase of the wave refraction.

[31] The “new” EMIC waves in the second row of Figure 8 are seen not only on the plasmopause, as expected from previous studies [e.g., *Horne and Thorne*, 1993; *Khazanov et al.*, 2006], but also inside and outside the plasmopause (see Figure 5, and compare Figure 8 with Figure 4). The latter feature in the wave spatial distributions is due to modification of the wave dispersive properties caused by RC  $H^+$  and not well observed when RC  $H^+$  is only included in the imaginary part of the wave dispersion relation (see Figure 8 and *Khazanov et al.* [2006]). This new theoretical finding is supported by the CRRES statistics reported by *Fraser and Nguyen* [2001], who found that EMIC waves in the inner magnetosphere are seen both inside and outside the plasmopause with a slight enhancement in wave power at the plasmopause.

[32] It follows from Figure 5 that RC  $H^+$  contributes only a few percent to the total plasma density near the inner edge of the plasmasphere boundary layer, but inclusion of RC  $H^+$  in the real part of the wave dispersion relation strongly affects the wave distribution on the plasmopause. This suggests that a slightly different plasmaspheric density model may result in a different wave distribution at the plasmopause. There is a qualitatively different situation outside the plasmopause where  $N_{RC}$  is comparable to  $N_e$  or even can strongly dominate thermal plasma (see Figures 4 and 5). Therefore it is unlikely that any reasonable modification to the thermal plasma model can make possible an appearance of EMIC waves outside the plasmopause without an inclusion of RC  $H^+$  in the real part of the wave dispersion relation. In addition, the storm-time magnetic field depression also can decrease the proton characteristic energy (see section 3) serving to increase an appearance of EMIC waves beyond the plasmopause. This effect should be seen in the results of the RAM-based simulations because RAM is now coupled with a self-consistent magnetic field calculation [e.g., *Zaharia et al.*, 2006].

## 7. Discussion

[33] *Engbreton et al.* [2007] presented measurements of EMIC waves in the Pc 1–2 frequency range and the associated ion distributions observed by Cluster during the October and November 2003 magnetic storms. The most intense waves were observed in the dawn sector for  $L = 4.4$ – $4.6$ ,  $MLat \approx 18^\circ$  on 22 November during 0825–0850 UT near the end of a rapid recovery phase. The waves were primarily transverse, propagating away from the equator, and predominantly left-hand polarized. Compared to the local proton gyrofrequency, these waves had a normalized frequency of  $X = 0.34$ , somewhat higher than

the local  $He^+$  gyrofrequency ( $X = 0.25$ ). A free energy to generate those waves was associated with anisotropic RC  $H^+$  of energies greater than 10 keV. Although the temperature anisotropy of these energetic protons was high during the entire 22 November pass, EMIC waves were observed only in conjunction with intensification by over an order of magnitude of the  $H^+$  fluxes below 1 keV. This suggests that the suprathermal plasma plays an important role in destabilization of a more energetic RC and/or plasma sheet  $H^+$ , and the high energy anisotropic RC and/or plasma sheet proton distributions appear to be a necessary but not sufficient condition for occurrence of EMIC waves. Similarly, studying Pc 1–2 events in the dayside outer magnetosphere, *Engbreton et al.* [2002] and *Arnoldy et al.* [2005] found that greatly increased fluxes of low energy protons were crucial for destabilization of the higher energy anisotropic RC protons. The analysis by *Engbreton et al.* [2007] suggests that the ion cyclotron wave growth rate could be significantly increased by the addition of cool/suprathermal  $H^+$  consistent with their observations. Their interpretation is in agreement with an idea of the present study (see section 3).

[34] The above satellite observations support our findings presented in Figure 8. Indeed, results in the first and second rows of Figure 8 are both obtained with RC  $H^+$  included in the imaginary part of the wave dispersion relation. It means that energetic anisotropic protons ( $E > 5$ – $10$  keV), which are able to resonantly interact with the  $He^+$ -mode EMIC waves, exist in both simulations with and without RC  $H^+$  in the real part of dispersion relation. Note that the number of resonant protons and their thermal anisotropy may be even smaller in the second row of Figure 8 compared to the first row because there are essentially more waves in the second row than in the first one. Therefore a major difference between two simulations is a difference in the total plasma density; the total plasma density in the second row of Figure 8 is increased by the RC  $H^+$  density compared to the first row in the figure. The density increase causes an increase of the wave growth rate that results in an additional EMIC wave occurrence in the second row of Figure 8 compared to the first row.

[35] The “new” waves in the dawn sector (see hour 28 in Figure 8) are caused by the suprathermal  $H^+$  with  $E \lesssim 2$  keV (see Figure 7a). This is in agreement with the observations by *Engbreton et al.* [2007], despite the fact that they observed EMIC waves outside the plasmopause but the “new” dawn waves in Figure 8 are generated on the plasmopause (see Figures 4 and 5a). On the other hand, all the “new” waves in the postnoon-premidnight MLT sector of Figure 8 are due to the density increase caused by the 10–100 keV RC  $H^+$  (see Figures 7b–7f). Although one may say that protons of these energies are not cool/suprathermal, it was shown in section 5 that RC  $H^+$  of such energies can be treated as “cold” in the real part of the  $He^+$ -mode EMIC wave dispersion relation. So the afternoon “new” waves in Figure 8 are also due to an addition of the “cold”  $H^+$ . Unfortunately, at present we do not know the observations that support our theoretical finding regarding EMIC wave generation in the postnoon-premidnight sector. It may be even difficult to experimentally separate the RC ions that are responsible for a resonant wave generation and those ions which modify the wave dispersion



properties because both these fractions have the same energies in the postnoon-premidnight MLT sector. It is likely that to do a such separation, a fine energy/pitch-angle structure of PSDF should be analyzed.

[36] Finally, we would like to recall that *Engebretson et al.* [2007] observed waves with a normalized frequency  $X = 0.34$ , whereas we considered the  $He^+$ -mode EMIC waves only, i.e., the waves with  $X < 0.25$ . (Note that the most intense burst of Pc 1 waves studied by *Arnoldy et al.* [2005] had a local normalized frequency  $X = 0.2$ , so the waves were on  $He^+$ -branch.) For the purpose of comparison with our previous results, in the present study we kept the ion percentage the same as before, i.e., 77%  $H^+$ , 20%  $He^+$ , and 3%  $O^+$ . Then the most effective generation takes place for the  $He^+$ -mode in the frequency range  $\Omega_{O^+} < \omega < \Omega_{He^+}$  [e.g., *Kozyra et al.*, 1984; *Horne and Thorne*, 1993; *Khazanov et al.*, 2003]. (Actually only waves on the left-hand polarized part of dispersive surface can grow and the corresponding wave frequencies should be in the range between the crossover frequency and  $\Omega_{He^+}$ .) The adopted ion content, however, differs strongly from the ion percentage reported by *Engebretson et al.* [2007]. On 22 November 2003 during 0740–0940 UT, they observed 81–89%  $H^+$ , 3%  $He^+$ , and 9–16%  $O^+$ , the qualitatively different percentage compared to the percentage used in our simulations. Such a great amount of  $O^+$ , in combination with a small amount of  $He^+$ , should suppress the  $He^+$ -mode and conversely favor the  $H^+$ -mode. A self-consistent modeling of the  $H^+$ -mode is well beyond the scope of the current study, and it should be done separately. At present, we believe that the crucial role of RC and/or the plasma sheet protons in destabilization of the high energy anisotropic RC protons is well established both experimentally and theoretically. We also think that this feature of the RC-EMIC wave interaction depends on the wave mode only quantitatively but the qualitative effect as such does not depend on the wave mode.

## 8. Conclusions

[37] In the present study, before employing a particular physical model for the wave energy propagation, we have analyzed three data sets in order to discriminate between the model of bouncing EMIC waves and the model of unidirectional wave propagation. Direct distinguishing between the wave packets bouncing between the off-equatorial magnetic latitudes, corresponding to the bi-ion hybrid frequencies in conjugate hemispheres, and unidirectional wave propagation may be done by analyzing the EMIC wave Poynting vector derived from observations. In the present study, we have analyzed the results of the most comprehensive study conducted by *Loto'aniu et al.* [2005]. We have analyzed the *Loto'aniu et al.* results twice. First time, we have employed the wave model that assumes an ion cyclotron instability region located near the equator with no reflecting boundaries off the equator (the first wave model). Second time, we have used the model that is the same as the first except waves are reflecting at the off-equatorial magnetic latitudes corresponding to the bi-ion hybrid frequencies in conjugate hemispheres (the second wave model). We have also analyzed the wave ellipticity from AMPTE/CCE [*Anderson et al.*, 1992b] and CRRES [*Fraser and Nguyen*, 2001]. This analysis allowed an

indirect discrimination between the first and second wave models. The results of our analysis can be summarized as follows:

[38] 1. Both the first and second wave models are equally consistent with the statistical results reported by *Loto'aniu et al.* [2005].

[39] 2. The first wave model is not consistent with a dynamic wave packet periodicity observed by *Loto'aniu et al.* [2005], while the second wave model is.

[40] 3. A combination of the first and second wave models is able to explain why the observed wave energy propagation was independent of the wave branch in the *Loto'aniu et al.* [2005] statistical results.

[41] 4. The first wave model is not consistent with the wave ellipticity observed in the near equatorial region, while the second wave model is.

[42] After the data analysis, it has been concluded that model of the wave packets bouncing between the off-equatorial magnetic latitudes, which correspond to the bi-ion hybrid frequencies in conjugate hemispheres, is justified and to a greater extent supported by the observations than the model of unidirectional wave propagation. This is why we used the second wave model in the present study.

[43] In this paper we have included RC  $H^+$  in the real part of EMIC wave dispersion relation and studied its effect on wave distribution during the storm. It is well known that plasma density is one of the most important characteristics controlling EMIC wave generation, and RC ions are usually included in the total density model in order to study the wave dispersive properties [e.g., *Kozyra et al.*, 1984; *Gamayunov et al.*, 1993]. Despite that, an assumption that the total plasma density is dominated by thermal plasma was made in previous efforts to model EMIC waves on a global magnetospheric scale [e.g., *Kozyra et al.*, 1997; *Jordanova et al.*, 2001, 2006; *Khazanov et al.*, 2006]. In other words, RC ions were only included in the imaginary part of the wave dispersion relation (in growth rate) but omitted in the real part of this relation. This assumption is especially severe outside the plasmapause where the RC density is comparable to or even dominates the thermal plasma density. Consequently, RC ions in the real part of the wave dispersion relation should affect the EMIC wave generation and its global distribution during the storm. This claim is strongly supported by the observations. Recent satellite observations of EMIC waves in the Pc 1–2 frequency range [*Engebretson et al.*, 2007] showed that although the temperature anisotropy of energetic ( $>10$  keV) RC protons was high during the entire 22 November 2003 perigee pass (in the dawn MLT sector at  $L \approx 4.5$ ), EMIC waves were observed only in conjunction with intensification of the ion fluxes below 1 keV by over an order of magnitude. This suggests that the suprathermal plasma ( $\lesssim 1$  keV) plays an important role in the destabilization of the more energetic RC and/or plasma sheet ions such that high energy anisotropic RC and/or plasma sheet proton distributions appear to be a necessary but not sufficient condition for occurrence of EMIC waves. Similar results were obtained for Pc 1–2 events in the dayside outer magnetosphere by *Engebretson et al.* [2002] and *Arnoldy et al.* [2005]. These observations provide clear evidence that both the cold plasmaspheric plasma and suprathermal ions injected from the plasma sheet control EMIC wave excita-

tion. Consequently, an inclusion of RC  $H^+$  in the real part of EMIC wave dispersion relation is needed for a more realistic wave simulation on the global magnetospheric scale.

[44] To demonstrate how an inclusion of RC  $H^+$  in the real part of the wave dispersion relation affects the  $He^+$ -mode EMIC waves, we have simulated the 2–3 May 1998 storm. The main findings from our simulations can be summarized as follows:

[45] 5. RC  $H^+$  contributes only a few percent to the total plasma density near the inner edge of the plasmasphere boundary layer but can dominate outside the plasmapause (except a dayside plasmaspheric drainage plume). About 90% of the RC  $H^+$  density in the dawn MLT sector is formed by the suprathermal ions with  $E \lesssim 2$  keV, while a major contribution in dusk comes from the 10–100 keV ions allowing not more than 10–20% for the suprathermal ions.

[46] 6. Including RC  $H^+$  in the real part of the wave dispersion relation increases local growth rate leading to a dramatic change in the wave global patterns. The “new” waves are generated not only on the plasmapause, as expected from previous global simulations, but also inside and outside the plasmapause consistent with the observations.

## Appendix A: Bouncing EMIC Wave Energy Versus Unidirectional Propagation: Observational Consideration

[47] An extended discussion about theoretical and observational bases of the model of EMIC waves bouncing between the off-equatorial magnetic latitudes, which correspond to the bi-ion hybrid frequencies in conjugate hemispheres, was recently published in JGR-Space Physics [Thorne and Horne, 2007; Khazanov *et al.*, 2007a]. Below, we continue by providing an additional data analysis, which could not be included in our paper [Khazanov *et al.*, 2007a] because of space limitation.

[48] Distinguishing between the wave packets bouncing between the off-equatorial magnetic latitudes, corresponding to the bi-ion hybrid frequencies in conjugate hemispheres, and unidirectional wave propagation may be done by analyzing the spatial-temporal distribution of the EMIC wave Poynting vector derived from observations [Erlandson *et al.*, 1990, 1992; Fraser *et al.*, 1992, 1996; LaBelle and Treumann, 1992; Mursula *et al.*, 2001; Loto'aniu *et al.*, 2005]. The most comprehensive statistical study based on 248 EMIC events was conducted by Loto'aniu *et al.* [2005], which is the focus of our analysis. To estimate a field-aligned component of the Poynting vector for EMIC waves in the Pc 1 frequency range, Loto'aniu *et al.* used three components of the wave magnetic field and two components of the electric field measured by CRRES. The observational data set covered about 10 months in the period 7 September 1990 through 9 October 1991, where most events were at higher L-shells and in the late afternoon MLT sector. Of the 248 events, 81 (33%) and 167 (67%) occurred above and below  $11^\circ$  |MLat|, respectively. Loto'aniu *et al.* reported bidirectional wave energy propagation, both away and toward the equator, for 26% of the events observed below  $11^\circ$  |MLat|, and unidirectional energy propagation away from the equator for all events outside  $\pm 11^\circ$  of the equator. The observed wave energy

propagation was independent of event frequency or wave branch.

[49] First, we interpret the Loto'aniu *et al.* results employing two qualitatively different physical models. The first wave model assumes an ion cyclotron instability region located near the equator with no reflecting boundaries off the equator. The second model is the same as the first except waves are reflecting at the off-equatorial magnetic latitudes corresponding to the bi-ion hybrid frequencies in conjugate hemispheres. Second, we present an analysis of the observed wave ellipticity, which allows indirect discrimination between the first and second wave models.

### A1. Poynting Flux Analysis Based on the First Wave Model

[50] It is obvious that in order for the first wave model to be applicable, the wave growth rate should be high enough to ensure wave amplification up to observable amplitudes during one pass through the unstable region. In the framework of this model, the seed fluctuations, irregularly emitted in one or both directions, will be amplified inside the instability region, and propagate either parallel or antiparallel to the magnetic field with equal probability. If the growth rate is high enough to allow an equatorward wave packet to amplify to observable levels before it reaches the equator, one would anticipate an irregularly bidirectional wave propagation inside some zone smaller than the equatorial instability region, but unidirectional wave propagation away from the equator otherwise. Note that, even inside this zone, bidirectional wave propagation will be only seen on an irregular basis but, on average, there is a unidirectional energy propagation away from the equator [see Loto'aniu *et al.*, 2005, Figure 4]. This is because the waves propagating away from the equator in both hemispheres, on average, have higher energy than the waves propagating toward the equator. Let us now estimate a latitudinal extent of the near equatorial instability region. To do so, we plot in Figure A1 the growth rate versus latitude for the  $He^+$ -mode EMIC waves. All the results shown are obtained from our RC-EMIC wave model (see section 2) at  $L = 6$  and MLT = 15 for hour 48 after 0000 UT on 1 May 1998. Depending on wave frequency, the growth rate has maximum at different magnetic latitudes ranging from  $0^\circ$  to  $17^\circ$ , where we assume that the boundary of the ion cyclotron instability region is located somewhere between  $10^\circ$  and  $20^\circ$  |MLat|. This estimate is consistent with calculations by Thorne and Horne [1997], so we use their results for the wave amplification rate. From their Figure 3b, one can obtain a wave gain rate of 5 dB/deg inside the near equatorial instability region. This suggests that a path-integrated gain of 50 dB may be attained during the equatorward wave propagation from  $20^\circ$  to  $10^\circ$ . This is enough to observe bidirectional wave propagation inside  $\pm 10^\circ$  of the equator, and unidirectional propagation outside this zone. This estimate matches the |MLat| =  $11^\circ$  boundary, which separates bidirectional and unidirectional wave propagation in the Loto'aniu *et al.* [2005] statistical results.

[51] Loto'aniu *et al.* found bidirectional wave energy propagation for only 26% of all events below  $11^\circ$  |MLat|. To interpret this we may assume that 60% of 167 wave packets observed below  $11^\circ$  |MLat| could not reach an observable amplitude during their propagation from the

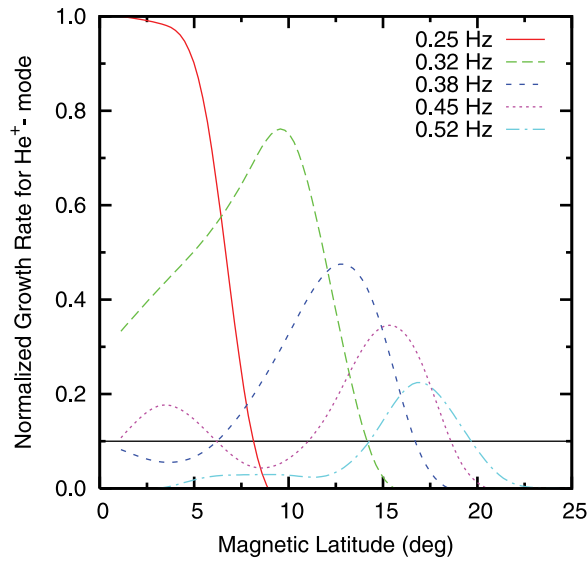


**Figure A1.** The normalized growth rate versus magnetic latitude for the field-aligned propagating  $He^+$ -mode EMIC waves. The RC is assumed to be entirely made up of energetic protons, and the thermal plasma consists of the cold electrons, 77%  $H^+$ , 20%  $He^+$ , and 3%  $O^+$ . All the results are taken from our simulation at  $L = 6$ , MLT = 15 for hour 48 after 0000 UT on 1 May 1998. The 10% level is marked by a horizontal line.

edge of instability region to the equator. Indeed, in the case when all the equatorward packets can be amplified by reaching  $|MLat| = 11^\circ$  (actually the specific satellite location during observation, which is in the range  $0^\circ \leq |MLat| < 11^\circ$ ), on average, we anticipate to find an oppositely directed partner for each wave packet observed inside  $\pm 11^\circ$  with an expectation probability of 2/3 (assuming that wave energy propagates equally backward and forward, or in both directions at the same time). In the opposite case when all the equatorward packets are not able to gain enough energy before they reach the satellite, the probability of bidirectional events is 0. Therefore the 26% may be explained as a result of 40:60 split between these two extremes.

[52] The above consideration shows that the first wave model is consistent with the Loto'aniu et al. statistical results. However, inconsistency remains with the wave packet periodicity reported by Loto'aniu et al. for some bidirectional events observed below  $11^\circ |MLat|$ . Since wave packet periodicity was not initially included in the first wave model, some modification to the model is required. (Recall that, in order to keep a qualitative difference between the first and second wave models, we are not allowed to introduce any reflecting surfaces in the first model.) Probably a simplest way to modify the model is to add ULF waves, which potentially are able to produce bidirectional repetition [e.g., Mursula et al., 2001]. Unfortunately, we cannot avoid the inconsistency by simply adding ULF waves to the first model. Indeed, Figure 3b of Loto'aniu et al. [2005] shows bidirectional wave propagation with a well-defined repetitive structure but, on average, the simultaneous compressional Pc 5 wave amplitudes were less than 0.3 nT. Therefore it is unlikely that bidirectional repetitive patterns are due to a modulation of

the plasma characteristics by Pc 5. It is possible, at least in principle, that periodic packets are a result of periodic wave generation, which is controlled by a group of resonant hot ions bouncing between the mirror points in the conjugate hemispheres [Erlandson et al., 1992]. However, this mechanism requires anomalous phase bunching of the ions, and it is unlikely that such spatially bunched bouncing ions can exist over time [Fraser et al., 1996]. Therefore we conclude that the first wave model is not consistent with a dynamical wave packet periodicity observed by Loto'aniu et al. [2005].

## A2. Poynting Flux Analysis Based on the Second Wave Model

[53] Now we reanalyze the Loto'aniu et al. [2005] results employing the second wave model. Note that reflection coefficient in the second model should be greater than zero, otherwise the second model is just identical to the first one. In order to avoid unnecessary complications, we first simplify the second model as much as possible: (1) only one quasimonochromatic EMIC wave packet propagates along a field line, bouncing between the off-equatorial magnetic latitudes corresponding to the bi-ion hybrid frequencies in conjugate hemispheres; (2) the field-aligned group velocity is assumed to be the Alfvén velocity, and to be coordinate independent; (3) the wave packet has duration  $\Delta T$ , length  $\Delta L$ , and a boxcar profile; (4) wave growth inside the near equatorial instability region is neglected, so wave energy may only decrease due to imperfect reflection (the reflection coefficient may include all possible loss mechanisms including wave tunneling/transformation, and resonant energy absorption by the thermal and hot plasmas). A sketch of the second wave model is shown in Figure A2. The coordinate  $z$  is measured along the field line with zero at the equator, the bi-ion reflecting surfaces are placed at  $\pm l$ , and a star marks the satellite location (see Figure A2a). Assuming an ideal instrument, which can instantly provide the Poynting vector of EMIC waves for a specified frequency, we plotted in Figures A2b and A2c a field-aligned component of the net Poynting vector as observed at two satellite locations. Recall that we assumed a quasimonochromatic wave packet, so the instantaneous measurements of the electric and magnetic wavefields allow us to calculate the Poynting flux for the known frequency. The only difference between measurements at these two locations is a partial, or total, overlap between the incident and reflected portions of the wave packet, observed in Figure A2c and lacking in Figure A2b. Since the wave reflection coefficient,  $R = S_r/S_i$ , is always less than 1, it follows from Figure A2c that a duration of the equatorward (reflected) wave signal decreases when the satellite approaches the reflection surface, while a duration of wave packet propagating away from the equator does not depend on  $z_s$ , being always  $\Delta T$ . In the limiting case  $z_s = -l$ , the equatorward signal disappears and only a poleward propagating signal may be observed. This preliminary consideration suggests that a finite time needed to obtain a single measurement of the Poynting vector may be a serious issue for detecting the equatorward wave propagation.

[54] The measurements of the electric and magnetic fields, taken at the instrument sampling rate, permit calculation of the total Poynting vector only. They provide no



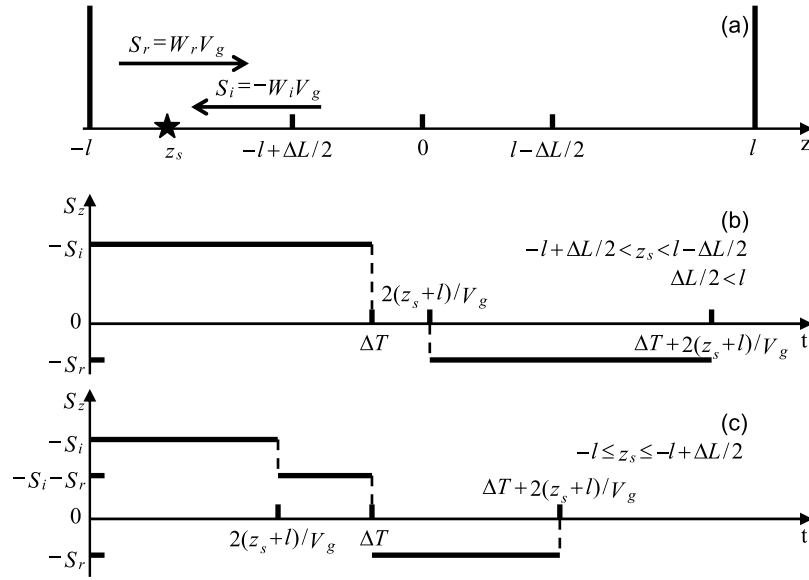


**Figure A2.** (a) Sketch of the second wave model (see text). The coordinate  $z$  is measured along the field line with zero at the equator. The bi-ion reflecting surfaces are located at  $\pm l$ , and a star marks satellite with coordinate  $z_s$ . The field-aligned wave group velocity and component of the incident (reflected) Poynting vector are  $V_g$  and  $S_i$  ( $S_r$ ), respectively. The incident (reflected) wave density is  $W_i$  ( $W_r$ ). (b and c) The field-aligned component of the net Poynting vector versus time as observed by perfect instrument at two satellite locations. The wave packet duration and length are  $\Delta T$  and  $\Delta L$ , respectively.

information regarding frequency-dependent effects, which are crucial for EMIC waves in a multi-ion magnetosphere. For example, it is possible for high frequency EMIC waves to reflect at the off-equatorial latitude where their frequency is close to the local bi-ion hybrid frequency. Particularly in  $H^+$ - $He^+$ - $O^+$  plasma, the  $He^+$ -mode and  $H^+$ -mode EMIC waves may reflect at the corresponding bi-ion latitudes while the  $O^+$ -mode EMIC waves can propagate to the Earth. Moreover, depending on the wave normal angle, even  $He^+$ -mode and  $H^+$ -mode can pass freely through the reflecting zone. Therefore to study the frequency and wave normal angle-dependent effects in wave propagation, the signal should be decomposed into constituent quasimonochromatic components. Fast Fourier Transform (FFT) analysis has become the conventional method for this purpose. The time window  $\Delta t_{FFT}$  used in the FFT analysis, is determined by the desired frequency resolution, which is the reciprocal of the window length. To achieve acceptable frequency resolution, time segments of one to several minutes or even much longer are typically used [e.g., Fraser, 1985; Ishida *et al.*, 1987; Loto'aniu *et al.*, 2005].

[55] The FFT analysis implies that the following combination of the electric and magnetic field has to be evaluated in order to estimate the Poynting flux at any particular time  $t$ :

$$\frac{\delta \mathbf{E}(t, \omega)}{\Delta t_{FFT}} \times \frac{\delta \mathbf{B}(t, \omega)}{\Delta t_{FFT}} = \frac{1}{(\Delta t_{FFT})^2} \int_{t-\Delta t_{FFT}/2}^{t+\Delta t_{FFT}/2} \delta \mathbf{E}(t_1) \exp(i\omega t_1) dt_1 \times \int_{t-\Delta t_{FFT}/2}^{t+\Delta t_{FFT}/2} \delta \mathbf{B}(t_2) \exp(i\omega t_2) dt_2. \quad (A1)$$

Both the electric and magnetic field signals may be decomposed as a superposition of components with different frequencies having slowly varying amplitudes as

functions of time. This implies that both integrals in equation (A1) are maximized for the resonant components, and we may take into account only these components in the total signals  $\delta \mathbf{E}(t_1)$  and  $\delta \mathbf{B}(t_2)$ . In other words, we may substitute  $\delta \mathbf{E}(t_1) \sim \delta \mathbf{E}_\omega(t_1) \exp(-i\omega t_1)$  and  $\delta \mathbf{B}(t_2) \sim \delta \mathbf{B}_\omega(t_2) \exp(-i\omega t_2)$  in equation (A1), where  $\delta \mathbf{E}_\omega(t_1)$  and  $\delta \mathbf{B}_\omega(t_2)$  are the slowly varying amplitudes of the field components corresponding to  $\omega$ . This gives

$$\begin{aligned} \frac{\delta \mathbf{E}(t, \omega)}{\Delta t_{FFT}} \times \frac{\delta \mathbf{B}(t, \omega)}{\Delta t_{FFT}} &\approx \frac{1}{(\Delta t_{FFT})^2} \int_{t-\Delta t_{FFT}/2}^{t+\Delta t_{FFT}/2} \delta \mathbf{E}_\omega(t_1) dt_1 \\ &\times \int_{t-\Delta t_{FFT}/2}^{t+\Delta t_{FFT}/2} \delta \mathbf{B}_\omega(t_2) dt_2 \approx \frac{1}{(\Delta t_{FFT})^2} \int_{t-\Delta t_{FFT}/2}^{t+\Delta t_{FFT}/2} \delta \mathbf{E}_\omega(t_1) \\ &\times \delta \mathbf{B}_\omega(t_1) dt_1. \end{aligned} \quad (A2)$$

Equation (A2) means that, in order to obtain the Poynting flux at time  $t$ , we have to average the signals shown in Figures A2b and A2c over a window  $\Delta t_{FFT}$  centered on  $t$ . The Poynting flux estimate is reliable only if we obtain a slowly varying result while shifting the FFT time window over an interval longer than  $\Delta t_{FFT}$ . In other words, the result should be slowly varying during the observational time  $\Delta t_{obs} = \Delta t_{FFT} + \tau$ , where  $\tau \gg 0$ . For example, Loto'aniu *et al.* [2005] used  $\Delta t_{FFT} = 50$  s, but the EMIC wave measurements were identified as a reliable event if both the electric and magnetic signals were continuously observed for at least  $\Delta t_{obs} = 60$  s. Keeping in mind these two facts, it follows immediately from Figures A2b and A2c that the equatorward Poynting flux only can be reliable if  $\Delta t_{FFT}$  does not exceed some limiting window length  $\Delta t_{max}$ . In other words, one is able to observe both the waves propagating away from and toward the equator if  $\Delta t_{FFT} < \Delta t_{max}$ , but only the wave packet propagating away from the

equator otherwise. In case  $\tau = 0$ , referring to Figures A2b and A2c, we can find this limiting window from the following equation:

$$\int_{\Delta T + 2(z_s + l)/V_g - \Delta t_{\max}}^{\Delta T + 2(z_s + l)/V_g} S_z(t) dt = 0,$$

which gives (recall that  $0 < R < 1$ ):

$$\frac{\Delta t_{\max}}{\Delta T} = \frac{2(z_s + l)}{\Delta L(1 - R)}, \text{ when } 2(z_s + l)/\Delta L \leq (1 - R), \quad (\text{A3})$$

and

$$\frac{\Delta t_{\max}}{\Delta T} = \frac{2(z_s + l)}{\Delta L} + R, \text{ when } 2(z_s + l)/\Delta L > (1 - R). \quad (\text{A4})$$

The case  $\tau \neq 0$  does not introduce any new physics in the model but rather makes analysis more complicated. It is for this reason that we examine equations (A3) and (A4), despite  $\tau = 10$  s in the paper of *Loto'aniu et al.* [2005]. Note that requirement  $\tau \neq 0$  decreases  $\Delta t_{\max}$  for any satellite location, on average, by  $1.5\tau - 2\tau$  compared to equations (A3) and (A4).

[56] Figure A3 shows  $\Delta t_{\max}/\Delta T$  versus  $2(z_s + l)/\Delta L$  for different reflection coefficients, where all the specified parameters, such as  $\Delta T$ ,  $\Delta L$ , and  $\Delta t_{FFT}$ , are taken from the paper by *Loto'aniu et al.* [2005]. For a given  $\Delta t_{FFT} = 50$  s, the intersection between the horizontal and colored lines in Figure A3 gives the “critical” satellite location which separates the low latitude region (in which both the poleward and equatorward Poynting vectors may be reliably measured) from a high latitude “blind” region (where only wave packet propagating away from the equator may be registered). If  $R = 0.01$ , for example, the equatorward Poynting flux may only be measured if  $\Delta l = (z_s + l) > 2.2 R_E$  for all three wave packets (“min,” “max,” and “av”) shown in Figure A3 (for the “av” wave packet, for example, substituting  $\Delta t_{\max} = \Delta t_{FFT} = 50$  s,  $\Delta T = \Delta T_{av} = 70$  s, and  $\Delta L = \Delta L_{av} = 6.1 R_E$  in equation (A3), we get the “critical” satellite location  $\Delta l_{av} = (z_s + l) = 2.2 R_E$ ). On the other hand, the bi-ion reflecting latitudes, whose location depends on EMIC wave frequency and ion composition, are typically located at  $|\text{MLat}| \approx 15\text{--}30^\circ$  [e.g., *Horne and Thorne*, 1993; *Khazanov et al.*, 2006; *Loto'aniu et al.*, 2005]. At  $L = 6$ , for example, these suggest that the satellite should be located inside of  $11^\circ |\text{MLat}|$  in order to “see” the reflected signal because the near equatorial field-aligned distance  $2.2 R_E$  corresponds to a latitudinal extent of about  $20^\circ$ . In such case, it is impossible to discriminate between the first and second wave models using the statistics of *Loto'aniu et al.* [2005]. In order to do that, we should be able to measure the reflected signal outside the near equatorial instability region. The ability to detect a small reflected signal outside  $|\text{MLat}| \approx 10\text{--}20^\circ$  is also crucial to resolve whether wave packets are bouncing between the off-equatorial bi-ion magnetic latitudes or whether there is only unidirectional wave propagation. Indeed, it was shown that wave amplification of 20–40 dB (factor of 10–100 in energy) may be attainable for the  $\text{He}^+$ -mode EMIC waves [*Hu and Fraser*, 1994]. In this case, a small reflected signal

may be reamplified while propagating through the near equatorial instability region and be observed by the satellite.

[57] For the range of reflection coefficients given in Figure A3, the “blind” region extends over  $\Delta l = 0.3\text{--}2.2 R_E$  and  $\Delta l = 0.02\text{--}2.2 R_E$  in the case of the “min” and “max” wave packet, respectively. In absence of any information regarding reflection coefficients, we average equations (A3) and (A4) over the entire possible range of the reflection coefficients, obtaining  $\langle \Delta l \rangle \approx 1.2 R_E$  for both wave packets (the same result can be obtained by substituting  $R = 0.5$  in equations (A3) and (A4)). Note that the Alfvén velocity increases toward the reflecting latitudes, suggesting an even greater wave packet length is possible than the estimate used and, as a result, a greater  $\langle \Delta l \rangle$  ( $\tau = 10$  s also increases  $\langle \Delta l \rangle$ ). So on average, the equatorward/reflected wave packet cannot be observed if the satellite is located closer to the reflection point than  $1.2 R_E$ , and only the packet propagating away from the equator may be observed there. In terms of latitude, taking  $L = 6$  as a typical L-shell, we have  $11^\circ$  as a width of the “blind” zone. Then, assuming  $|\text{MLat}| \approx 22^\circ$  as typical (an average) bi-ion reflecting latitude, we obtain that, on average, bidirectional wave energy propagation, both away and toward the equator, should be observed below  $11^\circ |\text{MLat}|$ , and only unidirectional energy propagation away from the equator outside  $\pm 11^\circ$  of the equator.

[58] The fact that *Loto'aniu et al.* [2005] found bidirectional wave energy propagation for only 26% of all events below  $11^\circ |\text{MLat}|$  may be interpreted similarly to that we did in the framework of the first wave model. Indeed, in the case when all the equatorward packets can be observed before they reach the actual satellite location, which is in the range  $0^\circ \leq |\text{MLat}| < 11^\circ$ , we expect an oppositely directed packet for each wave packet registered inside  $\pm 11^\circ$  with a probability of 1. In the opposite case when a combination of reflection coefficient, wave packet duration/length, and latitude of the reflecting surface does not allow the equatorward wave packets to be observed before they reach the satellite, the probability of a pair of bidirectional events is 0. Therefore the observed 26% may be explained as a result of an appropriate splitting between these two extreme conditions. So the analysis shows that the *Loto'aniu et al.* [2005] statistical results are consistent with the second wave model.

[59] Despite the second wave model is consistent with the *Loto'aniu et al.* [2005] statistics, the low frequency EMIC branch cannot be treated in the framework of this model. Indeed, there is no the bi-ion hybrid frequency for the  $O^+$ -mode EMIC waves in the  $H^+ \text{--} \text{He}^+ \text{--} O^+$  plasma, and this wave mode can freely propagate to the Earth. Due to the following energy absorption in the ionosphere, it is possible unidirectional propagation for this mode [e.g., *Erlandson et al.*, 1992], and this mode may be treated in the framework of the first wave model. It was shown in section A.1 that the first wave model is consistent with the *Loto'aniu et al.* statistics if the wave growth rate is high enough. Therefore the combination of the first and second wave models can explain why the observed wave energy propagation was independent of the wave branch in the *Loto'aniu et al.* statistical results.

[60] Let us now interpret the dynamical periodicity observed by *Loto'aniu et al.* [2005] for some bidirectional

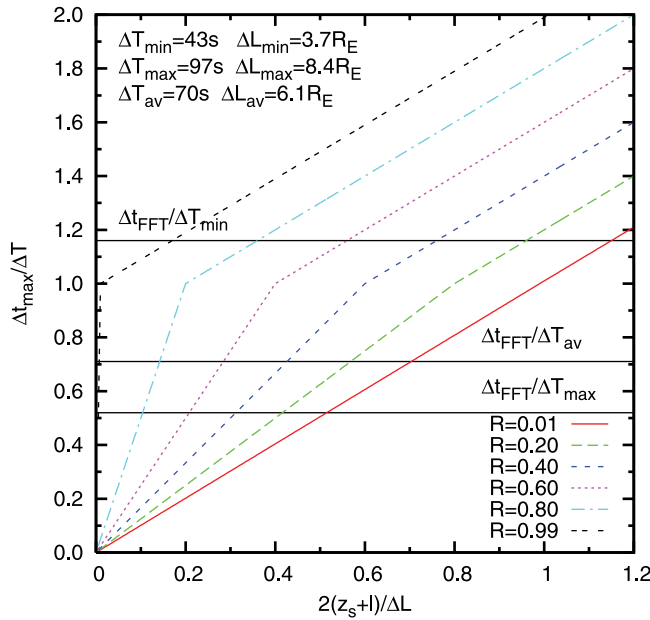


**Figure A3.** Normalized  $\Delta t_{\max}$  versus distance from the reflecting surface as specified by equations (A3) and (A4). The results are plotted for reflection coefficients in the range  $R = 0.01 - 0.99$ . The wave packet duration  $\Delta T_{\min}$  ( $\Delta T_{\max}$ ), and the length  $\Delta L_{\min}$  ( $\Delta L_{\max}$ ) are taken from Figure 3b by Loto'aniu et al. [2005], and  $R_E$  is the Earth's radius. The average wave packet duration and length are  $\Delta T_{av}$  and  $\Delta L_{av}$ , respectively. The reported Alfvén velocity of 550 km/s was used in order to estimate the wave packet lengths. The three horizontal lines show  $\Delta t_{FFT}/\Delta T_{\min}$ ,  $\Delta t_{FFT}/\Delta T_{av}$ , and  $\Delta t_{FFT}/\Delta T_{\max}$ , where  $\Delta t_{FFT} = 50$  s is the time window used by Loto'aniu et al.

events below  $11^\circ$  [MLat]. The wave packet oscillation is an internal feature of the second model, and all we are going to do at this point is to estimate the double-hop bounce period using this model, and then compare it with the experimental value. The wave packet transit time depends on the field-aligned distance between the off-equatorial bi-ion reflecting surfaces and wave group velocity, which depends on the ion composition and wave frequency. Unfortunately, most of this information is not available. For that reason, let us first estimate the double-hop bounce period using a constant Alfvén velocity of 550 km/s reported by Loto'aniu et al. for the events shown in their Figure 3b. Note that the Alfvén velocity was estimated assuming an electron-proton plasma. For  $L = 6$ , taking [MLat] =  $22^\circ$  as a typical bi-ion reflecting latitude, we get a theoretical bounce period of 107 s, which is 1.7 times smaller than 180 s, the average double-hop bounce period observed by Loto'aniu et al. This is not surprising because the field-aligned group velocity for EMIC waves is only the Alfvén velocity in the case of an electron-proton plasma at the zero frequency limit. Both the inclusion of heavy ions and a nonzero frequency correction will decrease the group velocity [e.g., Fraser, 1972] resulting in the increase of bounce period. For example, Fraser et al. [1989] found that the group propagation time was two times greater than the Alfvén time for the  $He^+$ -mode EMIC waves. Similar results were also reported by Arnoldy et al.

[2005] and Erlandson et al. [1992]. The factor two is more than enough to reconcile the above theoretical estimate with the observed double-hop bounce period. Therefore we conclude that the second wave model is consistent with the dynamical wave packet periodicity observed by Loto'aniu et al. [2005].

[61] The above quantitative analysis, although simplified, clearly demonstrates that a finite time needed to obtain a single measurement of the Poynting vector can be a serious problem in detecting the reflected/equatorward waves. Using instantaneous measurements of the electric and magnetic wavefield [e.g., Erlandson et al., 1990, 1992; Fraser et al., 1996; Mursula et al., 2001], we can reliably track the dynamics of the total Poynting flux but the contribution of the different frequencies is unclear. On the other hand, applying the FFT analysis to natural signal [e.g., Fraser et al., 1992; LaBelle and Treumann, 1992; Loto'aniu et al., 2005], we are able to resolve frequencies, but the extracted Poynting flux dynamics may be completely wrong for a particular frequency. There is a closely related problem in quantitative determination of the wave polarization and minimum variance direction for EMIC waves in the Earth's magnetosphere [Anderson et al., 1996]. In an attempt to resolve that problem, Anderson et al. developed a new approach, the "wave step technique," which operates on timescales of a few wave periods. Despite the working with very short time windows, it achieves good frequency precision. It is possible, therefore that one can achieve a better time-frequency balance in obtaining the EMIC wave Poynting vector by using the wave step technique. Another possible way to circumvent the problem may be to remove the selection criterion that qualitatively similar results should be obtained over intervals not less than  $\Delta t_{FFT}$ . This approach, although unreliable, will permit analysis of much shorter periods of the equatorward signal indicating the data set intervals that require special attention.

### A3. EMIC Wave Ellipticity: First Wave Model Versus Second Wave Model

[62] It is very difficult to locally generate highly oblique EMIC waves because the growth rate mainly maximizes for field-aligned waves (see Figure 1). Moreover, the strongest generation takes place in the near equatorial region (see Figure A1). This suggests that the greatest wave amplification takes place for the wave packets which have nearly field-aligned wave normals over the entire near equatorial unstable region. As a result, in the framework of the first wave model, where only a unidirectional wave propagation is permitted, one would anticipate seeing mainly quasi-field-aligned EMIC waves near the equator. Indeed, ray tracing calculations by Thorne and Horne [1997] and Horne and Thorne [1997] showed that to attain the greatest wave amplification the wave normal angle should be confined to less than  $10^\circ$  during wave propagation over the entire near equatorial region. On the other hand, wave reflection, included in the second wave model, results in the wave energy outflow to the region of higher wave normal angles [e.g., Horne and Thorne, 1993; Khazanov et al., 2006]. This makes possible to observe a mixture of oblique and field-aligned wave normals in the near equatorial zone. Therefore analysis of the wave normal angle distributions near the equator may discriminate between the first and second wave



model. Instead of analyzing wave normals, we may analyze the EMIC wave ellipticity, which is related to the wave normal angle. That is, if the plasma properties and wave frequency are specified, ellipticity determines wave normal angle, and vice versa for a plane EMIC wave. This is very helpful because there are very few satellite-based studies of EMIC waves that report wave normal angles, but great data sets of the wave ellipticity from AMPTE/CCE and CRRES [Anderson *et al.*, 1992b; Fraser and Nguyen, 2001]. The wave ellipticity is defined in the plane perpendicular to the external magnetic field as the ratio of the minor to the major axis of the wave polarization ellipse being  $-1$  for left circular,  $0$  for linear, and  $+1$  for right circular polarization. The model based expectations may be reformulated in the terms of ellipticity as follows: in the case of the first wave model, the ellipticity is expected to be close to  $-1$  in the near equatorial region while for model two, the near equatorial ellipticity is expected to be distributed between  $-1$  and some number around  $0$ .

[63] The CRRES statistics show that EMIC events near the magnetic equator are evenly distributed from left-hand polarized to linearly polarized with some right-hand polarized admixture [Fraser and Nguyen, 2001; Meredith *et al.*, 2003]. The statistical results from AMPTE/CCE are qualitatively the same in the prenoon-dusk MLT sector while waves at dawn are mostly linear polarized at all sampled latitudes, including the equator [Anderson *et al.*, 1992b]. It was emphasized by Anderson *et al.* [1992b] and Fraser and Nguyen [2001] that the observation of a significant number of linearly polarized events near the equator cannot be explained by polarization reversal from left-handed through linear to right-handed at the crossover frequency, as suggested by Young *et al.* [1981]. (Recall that if the Young *et al.* mechanism takes place then the quasi-field aligned waves can have a linear polarization.) Therefore the observed linear polarization inside the near equatorial zone suggests that waves should be often highly oblique. Using the more reliable wave step technique, Anderson *et al.* [1996] and Denton *et al.* [1996] analyzed data from the AMPTE/CCE spacecraft and presented the first results for near linearly polarized EMIC events. They indeed found a significant number of wave intervals where the wave normal angle was greater than  $70^\circ$ . The CRRES and AMPTE/CCE observations cannot be reconciled with the first wave model but have a natural explanation in the framework of the second model. The global EMIC wave simulation based on the second wave model [Khazanov and Gamayunov, 2007; Khazanov *et al.*, 2007b] showed that occurrences of the oblique and field-aligned wave normal angles are nearly equal near the equator with a slight dominance of oblique events consistent with observations.

[64] In conclusion we summarize the results of our analysis as follows: (1) both the first and second wave models are equally consistent with the statistical results reported by Loto'aniu *et al.* [2005]; (2) the first wave model is not consistent with the wave packet periodicity observed by Loto'aniu *et al.* [2005], while the second wave model is; (3) a combination of the first and second wave models can explain why the observed wave energy propagation was independent of the wave branch in the Loto'aniu *et al.* [2005] statistical results; (4) the first wave model is not

consistent with the wave ellipticity observed in the near equatorial region, while the second wave model is.

[65] **Acknowledgments.** We would like to thank M. Thomsen for providing LANL data. Funding in support of this study was provided by NASA grant UPN 370-16-10, NASA HQ POLAR Project and NASA LWS Program.

[66] Zuyin Pu thanks Mark Engebretson and another reviewer for their assistance in evaluating this paper.

## References

- Akhiezer, A. I., I. A. Akhiezer, R. V. Polovin, A. G. Sitenko, and K. N. Stepanov (1975a), *Plasma Electrodynamics*, vol. 1, Pergamon, Tarrytown, N. Y.
- Akhiezer, A. I., I. A. Akhiezer, R. V. Polovin, A. G. Sitenko, and K. N. Stepanov (1975b), *Plasma Electrodynamics*, vol. 2, Pergamon, Tarrytown, N. Y.
- Anderson, B. J., and S. A. Fuselier (1994), Response of thermal ions to electromagnetic ion cyclotron waves, *J. Geophys. Res.*, **99**, 19,413.
- Anderson, B. J., R. E. Erlandson, and L. J. Zanetti (1992a), A statistical study of Pc 1-2 magnetic pulsations in the equatorial magnetosphere: 1. Equatorial occurrence distributions, *J. Geophys. Res.*, **97**, 3075.
- Anderson, B. J., R. E. Erlandson, and L. J. Zanetti (1992b), A statistical study of Pc 1-2 magnetic pulsations in the equatorial magnetosphere: 2. Wave properties, *J. Geophys. Res.*, **97**, 3089.
- Anderson, B. J., R. E. Denton, and S. A. Fuselier (1996), On determining polarization characteristics of ion cyclotron wave magnetic field fluctuations, *J. Geophys. Res.*, **101**, 13,195.
- Angerami, J. J., and J. O. Thomas (1964), Studies of planetary atmospheres: 1. The distribution of ions and electrons in the earth's exosphere, *J. Geophys. Res.*, **69**, 4537.
- Arnoldy, R. L., *et al.* (2005), Pc 1 waves and associated unstable distributions of magnetospheric protons observed during a solar wind pressure pulse, *J. Geophys. Res.*, **110**, A07229, doi:10.1029/2005JA011041.
- Bräysy, T., K. Mursula, and G. Marklund (1998), Ion cyclotron waves during a great magnetic storm observed by Freja double-probe electric field instrument, *J. Geophys. Res.*, **103**, 4145.
- Chamberlain, J. W. (1963), Planetary corona and atmospheric evaporation, *Planet. Space Sci.*, **11**, 901.
- Clilverd, M. A., C. J. Rodger, R. M. Millan, J. G. Sample, M. Kokorowski, M. P. McCarthy, T. Ulich, T. Raita, A. J. Kavanagh, and E. Spanswick (2007), Energetic particle precipitation into the middle atmosphere triggered by a coronal mass ejection, *J. Geophys. Res.*, **112**, A12206, doi:10.1029/2007JA012395.
- Cornwall, J. M. (1965), Cyclotron instabilities and electromagnetic emission in the ultra low frequency and very low frequency ranges, *J. Geophys. Res.*, **70**, 61.
- Cornwall, J. M., F. V. Coroniti, and R. M. Thorne (1970), Turbulent loss of ring current protons, *J. Geophys. Res.*, **75**, 4699.
- Cornwall, J. M., F. V. Coroniti, and R. M. Thorne (1971), Unified theory of SAR arc formation at the plasmapause, *J. Geophys. Res.*, **76**, 4428.
- Daglis, I. A. (1997), The role of magnetosphere-ionosphere coupling in magnetic storm dynamics, in *Magnetic Storms*, *Geophys. Monogr. Ser.*, **98**, edited by B. T. Tsurutani *et al.*, p. 107, AGU, Washington, D. C.
- Denton, R. E., B. J. Anderson, G. Ho, and D. C. Hamilton (1996), Effects of wave superposition on the polarization of electromagnetic ion cyclotron waves, *J. Geophys. Res.*, **101**, 24,869.
- Engebretson, M. J., W. K. Peterson, J. L. Posch, M. R. Klatt, B. J. Anderson, C. T. Russell, H. J. Singer, R. L. Arnoldy, and H. Fukunishi (2002), Observations of two types of Pc 1-2 pulsations in the outer dayside magnetosphere, *J. Geophys. Res.*, **107**(A12), 1451, doi:10.1029/2001JA000198.
- Engebretson, M. J., A. Keiling, K.-H. Fornacon, C. A. Cattell, J. R. Johnson, J. L. Posch, S. R. Quick, K.-H. Glassmeier, G. K. Parks, and H. Réme (2007), Cluster observations of Pc 1-2 waves and associated ion distributions during the October and November 2003 magnetic storms, *Planet. Space Sci.*, **55**(6), 829.
- Erlandson, R. E., and A. J. Ukhorskiy (2001), Observations of electromagnetic ion cyclotron waves during geomagnetic storms: Wave occurrence and pitch angle scattering, *J. Geophys. Res.*, **106**, 3883.
- Erlandson, R. E., L. J. Zanetti, T. A. Potemra, L. P. Block, and G. Holmgren (1990), Viking magnetic and electric field observations of Pc 1 waves at high latitudes, *J. Geophys. Res.*, **95**, 5941.
- Erlandson, R. E., B. J. Anderson, and L. J. Zanetti (1992), Viking magnetic and electric field observations of periodic Pc 1 waves: Pearl pulsations, *J. Geophys. Res.*, **97**, 14,823.
- Farrugia, C. J., V. K. Jordanova, M. P. Freeman, C. C. Cochechi, R. L. Arnoldy, M. Engebretson, P. Stauning, G. Rostoker, M. F. Thomsen,

- G. D. Reeves, and K. Yumoto (2003), Large-scale geomagnetic effects of May 4, 1998, *Adv. Space Res.*, **31/4**, 1111.
- Fok, M.-C., J. U. Kozyra, A. F. Nagy, C. E. Rasmussen, and G. V. Khazanov (1993), A decay model of equatorial ring current and the associated aeronomical consequences, *J. Geophys. Res.*, **98**, 19,381.
- Fraser, B. J. (1972), Propagation of Pc 1 micropulsations in a proton-helium magnetosphere, *Planet. Space Sci.*, **20**, 1883.
- Fraser, B. J. (1985), Observations of ion cyclotron waves near synchronous orbit and on the ground, *Space Sci. Rev.*, **42**, 357.
- Fraser, B. J., and T. S. Nguyen (2001), Is the plasmopause a preferred source region of electromagnetic ion cyclotron waves in the magnetosphere?, *J. Atmos. Sol.-Terr. Phys.*, **63**, 1225.
- Fraser, B. J., W. J. Kemp, and D. J. Webster (1989), Ground-satellite study of a Pc 1 ion cyclotron wave event, *J. Geophys. Res.*, **94**, 11,855.
- Fraser, B. J., J. C. Samson, Y. D. Hu, R. L. McPherron, and C. T. Russell (1992), Electromagnetic ion cyclotron waves observed near the oxygen cyclotron frequency by ISEE 1 and 2, *J. Geophys. Res.*, **97**, 3063.
- Fraser, B. J., H. J. Singer, W. J. Hughes, J. R. Wygant, R. R. Anderson, and Y. D. Hu (1996), CRRES Poynting vector observations of electromagnetic ion cyclotron waves near the plasmopause, *J. Geophys. Res.*, **101**, 15,331.
- Fraser, B. J., H. J. Singer, M. L. Adrian, D. L. Gallagher, and M. F. Thomsen (2005), The relationship between plasma density structure and EMIC waves at geosynchronous orbit, in *Inner Magnetosphere Interactions: New Perspectives from Imaging*, *Geophys. Monogr. Ser.*, **159**, edited by J. L. Burch, M. Schulz, and H. Spence, p. 55, AGU, Washington, D. C.
- Fuselier, S. A., and B. J. Anderson (1996), Low-energy  $He^+$  and  $H^+$  distributions and proton cyclotron waves in the afternoon equatorial magnetosphere, *J. Geophys. Res.*, **101**, 13,255.
- Gamayunov, K. V., G. V. Khazanov, A. A. Veryaev, and T. I. Gombosi (1993), The effect of the hot, anisotropic magnetospheric protons on the dispersion relation, *Adv. Space Res.*, **4**, 121.
- Ganushkina, N. Yu., T. I. Pulkkinen, and T. Fritz (2005), Role of substorm-associated impulsive electric fields in the ring current development during storms, *Ann. Geophys.*, **23**, 579.
- Garcia, H. A., and W. N. Spjeldvik (1985), Anisotropy characteristics of geomagnetically trapped ions, *J. Geophys. Res.*, **90**, 347.
- Goldstein, J., J. L. Burch, B. R. Sandel, S. B. Mende, P. C. Sonnerup, and M. R. Hairston (2005), Coupled response of the inner magnetosphere and ionosphere on 17 April 2002, *J. Geophys. Res.*, **110**, A03205, doi:10.1029/2004JA010712.
- Gonzalez, W. D., B. T. Tsurutani, A. L. C. Gonzalez, E. J. Smith, F. Tang, and S.-I. Akasofu (1989), Solar wind-magnetosphere coupling during intense magnetic storms (1978–1979), *J. Geophys. Res.*, **94**, 8835.
- Gorbachev, O. A., G. V. Khazanov, K. V. Gamayunov, and E. N. Krivorutsky (1992), A theoretical model for the ring current interaction with the Earth's plasmasphere, *Planet. Space Sci.*, **40**, 859.
- Hamilton, D. C., G. Gloeckler, F. M. Ipavich, W. Studemann, B. Wilken, and G. Kremser (1988), Ring current development during the great geomagnetic storm of February 1986, *J. Geophys. Res.*, **93**, 14,343.
- Haselgrove, J. (1954), Ray theory and a new method for ray tracing, *Report of Conference on the Physics of the Ionosphere*, London: Physical Society, 355.
- Haselgrove, C. B., and J. Haselgrove (1960), *Twisted ray paths in the ionosphere*, *Proc. Phys. Soc.*, **75**, 357, London.
- Horne, R. B., and R. M. Thorne (1993), On the preferred source location for the convective amplification of ion cyclotron waves, *J. Geophys. Res.*, **98**, 9233.
- Horne, R. B., and R. M. Thorne (1997), Wave heating of  $He^+$  by electromagnetic ion cyclotron waves in the magnetosphere: Heating near  $H^+$ - $He^+$  bi-ion resonance frequency, *J. Geophys. Res.*, **102**, 11,457.
- Hu, Y. D., and B. J. Fraser (1994), Electromagnetic ion cyclotron wave amplification and source regions in the magnetosphere, *J. Geophys. Res.*, **99**, 263.
- Ishida, J., S. Kokubun, and R. L. McPherron (1987), Substorm effects on spectral structures of Pc 1 waves at synchronous orbit, *J. Geophys. Res.*, **92**, 143.
- Jordanova, V. K., L. M. Kistler, J. U. Kozyra, G. V. Khazanov, and A. F. Nagy (1996), Collisional losses of ring current ions, *J. Geophys. Res.*, **101**, 111.
- Jordanova, V. K., C. J. Farrugia, L. Janoo, J. M. Quinn, R. B. Torbert, K. W. Ogilvie, R. P. Lepping, J. T. Steinberg, D. J. McComas, and R. D. Belian (1998), October 1995 magnetic cloud and accompanying storm activity: Ring current evolution, *J. Geophys. Res.*, **103**, 79.
- Jordanova, V. K., C. J. Farrugia, R. M. Thorne, G. V. Khazanov, G. D. Reeves, and M. F. Thomsen (2001), Modeling ring current proton precipitation by EMIC waves during the May 14–16, 1997, storm, *J. Geophys. Res.*, **106**, 7.
- Jordanova, V. K., Y. S. Miyoshi, S. Zaharia, M. F. Thomsen, G. D. Reeves, D. S. Evans, C. G. Mouikis, and J. F. Fennell (2006), Kinetic simulations of ring current evolution during the Geospace Environment Modeling challenge events, *J. Geophys. Res.*, **111**, A11S10, doi:10.1029/2006JA011644.
- Kennel, C. F., and H. E. Petschek (1966), Limit on stably trapped particle fluxes, *J. Geophys. Res.*, **71**, 1.
- Khazanov, G. V., and K. V. Gamayunov (2007), Effect of electromagnetic ion cyclotron wave normal angle distribution on relativistic electron scattering in outer radiation belt, *J. Geophys. Res.*, **112**, A10209, doi:10.1029/2007JA012282.
- Khazanov, G. V., K. V. Gamayunov, and V. K. Jordanova (2003), Self-consistent model of magnetospheric ring current ions and electromagnetic ion cyclotron waves: The 2–7 May 1998 storm (2003), *J. Geophys. Res.*, **108**(A12), 1419, doi:10.1029/2003JA009856.
- Khazanov, G. V., K. V. Gamayunov, D. L. Gallagher, and J. U. Kozyra (2006), Self-consistent model of magnetospheric ring current and propagating electromagnetic ion cyclotron waves: Waves in multi ion magnetosphere, *J. Geophys. Res.*, **111**, A10202, doi:10.1029/2006JA011833.
- Khazanov, G. V., K. V. Gamayunov, D. L. Gallagher, and J. U. Kozyra (2007a), Reply to comment by R. M. Thorne and R. B. Horne on Khazanov et al. [2002] and Khazanov et al. [2006], *J. Geophys. Res.*, **112**, A12215, doi:10.1029/2007JA012463.
- Khazanov, G. V., K. V. Gamayunov, D. L. Gallagher, J. U. Kozyra, and M. W. Liemohn (2007b), Self-consistent model of magnetospheric ring current and propagating electromagnetic ion cyclotron waves: 2. Wave induced ring current precipitation and thermal electron heating, *J. Geophys. Res.*, **112**, A04209, doi:10.1029/2006JA012033.
- Kimura, I. (1966), Effects of ions on whistler-mode ray tracing, *Radio Sci.*, **1**, 269.
- Kozyra, J. U., T. E. Cravens, A. F. Nagy, E. G. Fonthelm, and R. S. B. Ong (1984), Effects of energetic heavy ions on electromagnetic ion cyclotron wave generation in the plasmopause region, *J. Geophys. Res.*, **89**, 2217.
- Kozyra, J. U., V. K. Jordanova, R. B. Horne, and R. M. Thorne (1997), Modeling of the contribution of Electromagnetic Ion Cyclotron (EMIC) waves to stormtime ring current erosion, in *Magnetic Storms*, *Geophys. Monogr. Ser.*, vol. 98, edited by B. T. Tsurutani et al., p. 187, AGU, Washington, D. C.
- LaBelle, J., and R. A. Treumann (1992), Poynting vector measurements of electromagnetic ion cyclotron waves in the plasmasphere, *J. Geophys. Res.*, **97**, 13,789.
- Lorentzen, K. R., M. P. McCarthy, G. K. Parks, J. E. Foat, R. M. Millan, D. M. Smith, R. P. Lin, and J. P. Treilhou (2000), Precipitation of relativistic electrons by interaction with electromagnetic ion cyclotron waves, *J. Geophys. Res.*, **105**, 5381.
- Loto'aniu, T. M., B. J. Fraser, and C. L. Waters (2005), Propagation of electromagnetic ion cyclotron wave energy in the magnetosphere, *J. Geophys. Res.*, **110**, A07214, doi:10.1029/2004JA010816.
- Lyons, L. R., and D. J. Williams (1984), *Quantitative Aspects of Magnetospheric Physics*, D. Reidel, Dordrecht.
- Maynard, N. C., and A. J. Chen (1975), Isolated cold plasma regions: Observations and their relation to possible production mechanisms, *J. Geophys. Res.*, **80**, 1009.
- Meredith, N. P., R. M. Thorne, R. B. Horne, D. Summers, B. J. Fraser, and R. R. Anderson (2003), Statistical analysis of relativistic electron energies for cyclotron resonance with EMIC waves observed on CRRES, *J. Geophys. Res.*, **108**(A6), 1250, doi:10.1029/2002JA009700.
- Mishin, E. V., and W. J. Burke (2005), Stormtime coupling of the ring current, plasmasphere and topside ionosphere: Electromagnetic and plasma disturbances, *J. Geophys. Res.*, **110**, A07209, doi:10.1029/2005JA011021.
- Mishin, E. V., and V. M. Mishin (2007), Prompt response of SAPS to stormtime substorms, *J. Atmos. Sol.-Terr. Phys.*, **69**, 1233.
- Mursula, K., T. Bräysy, K. Niskala, and C. T. Russell (2001), Pc 1 pearls revised: Structured electromagnetic ion cyclotron waves on Polar satellite and on ground, *J. Geophys. Res.*, **106**, 29,543.
- Rairden, R. L., L. A. Frank, and J. D. Craven (1986), Geocoronal imaging with dynamics explorer, *J. Geophys. Res.*, **91**, 13,613.
- Rasmussen, C. E., S. M. Guiter, and S. G. Thomas (1993), Two-dimensional model of the plasmasphere: Refilling time constants, *Planet. Space Sci.*, **41**, 35.
- Sandanger, M., F. Soraas, K. Aarsnes, K. Oksavik, and D. S. Evans (2007), Loss of relativistic electrons: Evidence for pitch angle scattering by electromagnetic ion cyclotron waves excited by unstable ring current protons, *J. Geophys. Res.*, **112**, A12213, doi:10.1029/2006JA012138.
- Sheldon, R. B., and D. C. Hamilton (1993), Ion transport and loss in the Earth's quiet ring current: 1. Data and standard model, *J. Geophys. Res.*, **98**, 13,491.
- Stern, D. P. (1975), The motion of a proton in the equatorial magnetosphere, *J. Geophys. Res.*, **80**, 595.

- Stix, T. H. (1992), *Waves in Plasmas*, Am. Inst. of Phys., College Park, MD.
- Summers, D., and R. M. Thorne (2003), Relativistic electron pitch-angle scattering by electromagnetic ion cyclotron waves during geomagnetic storms, *J. Geophys. Res.*, *108*(A4), 1143, doi:10.1029/2002JA009489.
- Thorne, R., and R. Horne (1994), Energy transfer between energetic ring current  $H^+$  and  $O^+$  by electromagnetic ion cyclotron waves, *J. Geophys. Res.*, *99*, 17,275.
- Thorne, R., and R. Horne (1997), Modulation of electromagnetic ion cyclotron instability due to interaction with ring current  $O^+$  during the geomagnetic storms, *J. Geophys. Res.*, *102*, 14,155.
- Thorne, R. M., and R. B. Horne (2007), Comment on Khazanov et al. [2002] and Khazanov et al. [2006], *J. Geophys. Res.*, *112*, A12214, doi:10.1029/2007JA012268.
- Tsyganenko, N. A., H. J. Singer, and J. C. Kasper (2003), Storm-time distortion of the inner magnetosphere: How severe can it be?, *J. Geophys. Res.*, *108*(A5), 1209, doi:10.1029/2002JA009808.
- Volland, H. (1973), A semiempirical model of large-scale magnetospheric electric fields, *J. Geophys. Res.*, *78*, 171.
- Young, D. T., S. Perraut, A. Roux, C. de Villedary, R. Gendrin, A. Korth, G. Kremser, and D. Jones (1981), Wave-particle interactions near  $\Omega_{He^+}$  observed on GEOS 1 and 2: 1. Propagations of ion cyclotron waves in  $He^+$ -rich plasma, *J. Geophys. Res.*, *86*, 6755.
- Young, D. T., H. Balsiger, and J. Geiss (1982), Correlations of magnetospheric ion composition with geomagnetic and solar activity, *J. Geophys. Res.*, *87*, 9077.
- Zaharia, S., V. K. Jordanova, M. F. Thomsen, and G. D. Reeves (2006), Self-consistent modeling of magnetic fields and plasmas in the inner magnetosphere: Application to a geomagnetic storm, *J. Geophys. Res.*, *111*, A11S14, doi:10.1029/2006JA011619.

---

K. V. Gamayunov, National Space Science and Technology Center, NASA Marshall Space Flight Center, Space Science Department, Universities Space Research Association, 320 Sparkman Drive, Huntsville, AL 35805, USA. (konstantin.gamayunov-1@nasa.gov)

G. V. Khazanov, NASA, Goddard Space Flight Center, Greenbelt, MD, USA. (george.v.khazanov@nasa.gov)